nature nanotechnology

ARTICLES

https://doi.org/10.1038/s41565-021-00947-8

Check for updates

Progressive growth of the solid–electrolyte interphase towards the Si anode interior causes capacity fading

Yang He[1,7,8], Lin Jiang[2,8], Tianwu Chen[3,8], Yaobin Xu[1,8], Haiping Jia[4,8], Ran Yi[4,8], Dingchuan Xue[3], Miao Song[5], Arda Genc[2], Cedric Bouchet-Marquis[2], Lee Pullan[2], Ted Tessner[2], Jinkyoung Yoo[6]✉, Xiaolin Li[4]✉, Ji-Guang Zhang[4], Sulin Zhang[3]✉ and Chongmin Wang[1]✉

The solid–electrolyte interphase (SEI), a layer formed on the electrode surface, is essential for electrochemical reactions in batteries and critically governs the battery stability. Active materials, especially those with extremely high energy density, such as silicon (Si), often inevitably undergo a large volume swing upon ion insertion and extraction, raising a critical question as to how the SEI interactively responds to and evolves with the material and consequently controls the cycling stability of the battery. Here, by integrating sensitive elemental tomography, an advanced algorithm and cryogenic scanning transmission electron microscopy, we unveil, in three dimensions, a correlated structural and chemical evolution of Si and SEI. Corroborated with a chemomechanical model, we demonstrate progressive electrolyte permeation and SEI growth along the percolation channel of the nanovoids due to vacancy injection and condensation during the delithiation process. Consequently, the Si–SEI spatial configuration evolves from the classic 'core–shell' structure in the first few cycles to a 'plum-pudding' structure following extended cycling, featuring the engulfing of Si domains by the SEI, which leads to the disruption of electron conduction pathways and formation of dead Si, contributing to capacity loss. The spatially coupled interactive evolution model of SEI and active materials, in principle, applies to a broad class of high-capacity electrode materials, leading to a critical insight for remedying the fading of high-capacity electrodes.

It has been almost two decades since the lithium-ion battery brought us the rechargeable world. The megatrend of electrification of our society, including the demand to power long-range electric vehicles, intelligent robots and powerful portable electronics and to improve the resiliency and reliability of electrical grids, has put continuous requirements on next-generation Li-ion batteries. Integration of new electrode materials, in terms of cycling stability, is often dictated by interaction between the materials and the associated working environment, which is manifested by an interlayer between the active material and the electrolyte[1,2], that is, the SEI. Nevertheless, the understanding of how the SEI evolves during cycling and leads to capacity fading remains conjectural.

For instance, due to its high gravimetric capacity, low voltage window (~0.01–1 V versus a Li/Li^+ electrode), low price and natural abundance, Si has been perceived by both the scientific community and industries as the most promising high-capacity anode material for practical application in next-generation Li-ion batteries[3,4]. Tremendous ingenious nanoscale engineering concepts have emerged in the past decade[5–8], intending to tackle the barrier associated with the volume expansion of Si and consequently mitigating the capacity fading of Si-based anode materials[2,4,9–11]. However, large-scale application of Si as an anode for Li-ion batteries remains a challenge and requires a clear understanding of the underlying fading mechanism of the nanosized Si (refs. [4,5,12]).

It is generally conjectured that the capacity fading of Si originates in the intrinsic large volume changes and ensuing accumulation of the SEI with repeated cycling, as commonly anticipated for this class of materials. Typically, the volume change will lead to cracking of Si (ref. [13]); crumpling, regeneration and accumulative growth of the SEI; and attendant loss of electrical contact[3,14]. This view appears to be self-consistent for explaining the capacity fading of Si with sizes larger than a critical dimension of typically 150 nm, but fails in reconciliation with the capacity fading of nanosized Si (refs. [3,15]), wherein the material cracking issue is effectively attenuated by the reduced particle size[3,16,17]. Electrode-level failure aside[18], the capacity fading of nanosized Si has been related, more or less hypothetically, to the thickening of the SEI layer on the material surface[2,19–21], progressive loss of active materials such as Si and Li (refs. [22,23]) and electrochemical–mechanical degradation[24]. However, key experimental evidence is still lacking on the dynamic evolution of SEI, both structural and chemical, in response to the large volume swing of electrodes during cycling.

Current direct observations of the SEI are largely based on the two-dimensional projection imaging and energy dispersive X-ray spectroscopy (EDS) mapping of elements[20,25], which are unable to correlate with the three-dimensional (3D) structural evolution of the nanosized Si. Electron tomography is a technique that retrieves the 3D structural information of nanoscale objects from

[1]Environmental Molecular Sciences Laboratory, Pacific Northwest National Laboratory, Richland, WA, USA. [2]Materials and Structural Analysis Division, Thermo Fisher Scientific, Hillsboro, OR, USA. [3]Department of Engineering Science and Mechanics, Pennsylvania State University, University Park, PA, USA. [4]Energy and Environmental Directorate, Pacific Northwest National Laboratory, Richland, WA, USA. [5]Physical and Computational Science Directorate, Pacific Northwest National Laboratory, Richland, WA, USA. [6]Center for Integrated Nanotechnologies, Los Alamos National Laboratory, Los Alamos, NM, USA. [7]Present address: Beijing University of Science and Technology, Beijing, China. [8]These authors contributed equally: Yang He, Lin Jiang, Tianwu Chen, Yaobin Xu, Haiping Jia, Ran Yi. ✉e-mail: jyoo@lanl.gov; xiaolin.li@pnnl.gov; suz10@psu.edu; chongmin.wang@pnnl.gov

a tilt series of two-dimensional projections[26], a technique that has been pushed to image materials at the atomic level in three dimensions[27]. However, electron tomography on cycled electrode materials has been challenging due to the severe damage from the high electron dose necessary for electron tomography imaging. Inspired by the studies of structural biology[28] and cryogenic transmission electron microscopy (cryo-TEM) for Li dendrites[29,30], we hold the sample at cryogenic temperature during preparation and imaging to minimize the sample damage from air and the imaging beam. Additionally, we employ an advanced reconstruction algorithm that enables capturing the tomography tilt series with a further reduced electron dose. These approaches preserve the lightweight materials encompassed by the SEI for the high-resolution electron tomography imaging of both the structure and chemical compositions, as detailed in the Methods.

Herein, we integrate advanced EDS tomography, cryogenic scanning transmission electron microscopy (cryo-STEM) and chemomechanical modelling to show, explicitly in three dimensions, the correlated structural and chemical evolution of the SEI and Si. Specifically, we discover the progressive growth of the SEI towards the Si interior as the Si nanowires become porous with cycling. As such, the otherwise pure Si eventually evolves into a mixture of Si and SEI with a 'plum-pudding' structure. We reveal that the origin of such a structural evolution is rooted in the formation of voids due to vacancy condensation during the delithiation process. This discovery unravels beyond the fading mechanisms associated with the large volume change of Si—the intrinsic fading mechanism of the capacity of Si as a Li host—and, in principle, applies to a broad class of electrode materials featuring large volume changes upon ion insertion and extraction.

Results and discussion

Correlated evolution of Si and SEI. A half-cell coin-cell set-up is used for the electrochemical cycling. Details on the cell assembly and electrochemical test are included in the Methods. Si nanowires directly grown on a stainless-steel plate are used as the electrode (Fig. 1a). This unique set-up allows us to attribute the cell capacity fading primarily to the fading of Si due to following reasons. First, the bulk Li metal counter-electrode provides an excessive Li-ion source for the cycling, eliminating the cell capacity fading by the draining of Li and degradation of the cathode in a full cell; second, the electrolyte loading is in a flooded mode to avoid electrolyte depletion along cycling; and third, the good mechanical and electrical contact between the stainless steel and the Si nanowires eliminates the need for the addition of binder and conductive materials, which otherwise would contribute to fading through electrode-level failure by the loss of electrical contact between the active materials and the current collector[15,18].

Since the nanowires are soaked in the liquid electrolyte, lithiation of the Si nanowires starts from the side surface, forming a core–shell structure wherein crystalline Si is the core and the amorphous Li_xSi is the shell (Fig. 1b–d). Note that a SEI layer also forms during the first lithiation as an additional shell on the Si nanowire. The whole electrode demonstrates typical capacity fading and Coulombic efficiency with cycling (Fig. 1e and Supplementary Figs. 1–3). The nanowires used in this study have a diameter range of ~60–90 nm, which is smaller than the critical diameter of ~150 nm and hence should not fracture upon cycling[16,31]. To unravel the SEI evolution and capacity-fading mechanism, we deliberately retrieved the delithiated nanowires in their 'as-cycled' state (Methods for details) and studied the structural and chemical evolution of Si and the SEI and their spatial correlation with the progress of cycling.

One of the notable features of the Si nanowires with cycling is the gradual loss of the original wire-shaped uniformity and the topographic roughening of the original smooth Si surface, as shown in Fig. 1f–i and Supplementary Fig. 4. Furthermore, the Si nanowires become porous, and the pore size and total volume apparently increase with increasing number of cycles, as illustrated by the cryo-STEM high-angle annular dark field (cryo-STEM-HAADF) images in Fig. 1f–i, where the pores are imaged as a dark contrast (Supplementary Fig. 5). The formation of pores therein is a direct consequence of the vacancies condensation due to Li^+ extraction[32]. Thermodynamically, the vacancies prefer to annihilate at the Si surface[32–34], leading to the roughening of the Si surface, which was attributed previously to material loss[22] (Supplementary Discussion).

The structural evolution of Si is concomitant with the SEI formation on the Si nanowire. The evolving nature of the spatial correlation between the Si and the SEI layer is vividly demonstrated in Figs. 2–4 through cryo-STEM-HAADF imaging and EDS tomography of the nanowires following the 1st, 36th and 100th cycles. Figure 2 shows elemental composition mapping data that are extracted from the tilt series of the EDS tomography. After the first cycling, the SEI formed on the Si is composed of fluorine (F), oxygen (O), carbon (C) and trivial phosphorus (P) and morphologically features a thin layer of ~20 nm in thickness (Fig. 2a), which appears to be consistent with the classic model of the core–shell structure. Though the core–shell structure remains after the 36th cycle, the Si core becomes more porous with a rough surface (Fig. 2b), which is in stark contrast to the well-defined surface of the pristine Si (Fig. 1f) and the relatively smooth surface of Si following the first cycle. After the 100th cycling, the Si and SEI are no longer clearly defined as a core–shell structure; instead, the Si and SEI are apparently mixed together to form a composite structure, a vivid analogy of a plum pudding, as shown in Fig. 2c.

Such evolution of the spatial correlation between the Si and SEI layer is further demonstrated in three dimensions through EDS tomography as shown in Figs. 3 and 4. Figure 3 shows EDS tomography of the elemental composition of a 36th-cycle Si nanowire with the SEI shell. In contrast to the highly destructed morphology of the nanowires reported in the literature[3,24], the 'as-cycled' sample still retains an overall nanowire morphology. More importantly, the SEI is not a uniform coating layer. Additionally, measurements of the SEI thickness on the nanowire based on the cryo-STEM-HAADF images (Supplementary Figs. 6–8) indicate that the SEI shell forms largely in the first cycle, and its growth slows thereafter. These findings suggest that the growth mode of the SEI is more complicated than the conventional idea that the SEI uniformly and continuously thickens at the outer surface of the nanowires with cycling.

Furthermore, cross-sectional segmentation analysis of the 3D chemical composition of the nanowire reveals a gradual growth of the SEI towards the Si interior with cycling. As shown in Fig. 4a,d,g, Supplementary Videos 1 and 2 and Supplementary Fig. 9, the first-cycle nanowire has a well-defined core–shell structure with a pure Si core. By contrast, elements from the electrolyte start to breach the core and appear in the pores after 36 cycles (Fig. 4b,e,h, Supplementary Videos 3 and 4 and Supplementary Fig. 10). After 100 cycles, the Si becomes highly mixed with the SEI, resembling the plum-pudding structure (Fig. 4c,f,i, Supplementary Videos 5 and 6 and Supplementary Fig. 11), with weakly connected Si domains (plums) embedded in the SEI matrix (pudding). Such correlated evolution of the SEI and Si can be correlated to the intrinsic structural deterioration of Si with cycling. Channels winding from the Si nanowire surface into the core can be created as the surface pits and internal pores connect, as evidenced by the STEM tomography images of the cycled nanowire in Supplementary Fig. 4. These channels can facilitate permeation of the electrolyte molecules through the weakened SEI shell during cycling[23–25,35,36] and lead to the SEI growth towards the interior of the Si nanowire. It is apparent that the SEI as a layer is well defined for the first cycle. However, with increasing numbers of cycles, as we observed here, the SEI and Si gradually mingle. It has been shown that the SEI on

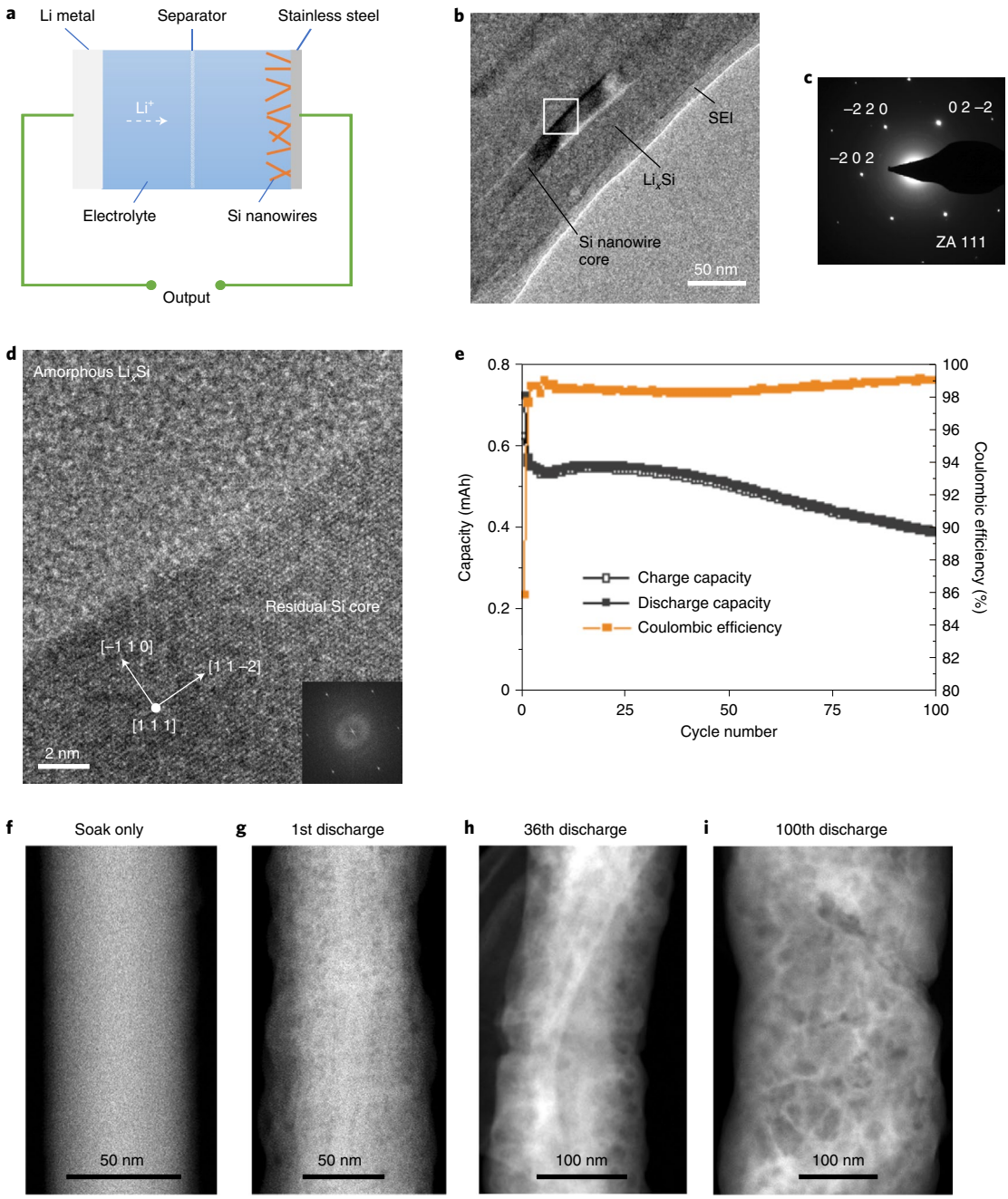

Fig. 1 | Experimental set-up, battery performance and structural evolution of Si. a, Schematic of the coin-cell set-up. **b**, Cryo-TEM images of a Si nanowire during the first lithiation. **c**, Electron diffraction pattern of the nanowire showing the single-crystalline nature of the remaining crystalline Si (ZA stands for zone axis). **d**, High-resolution image of the boxed region in **b** showing the lattice of the remaining Si core and the amorphous Li_xSi, where the inset is the fast Fourier transform of the image, indicating that the zone axis is [111]. **e**, Capacity and Coulombic efficiency evolutions with cycle numbers. **f**–**i**, Cryo-STEM-HAADF images of the Si nanowires at different cycle numbers: fresh Si nanowire prior to 1st lithiation, which was only soaked in the electrolyte (**f**), 1st delithiated (**g**), 36th delithiated (**h**) and 100th delithiated (**i**). Note that these are representative images of different nanowires. With the progression of the cycling, Si becomes porous.

Si is dynamic and changes with the state of the charge[25]. What we observed here regarding the growth of the SEI towards the interior of the Si is mediated by pore formation due to Li vacancy condensation during each cycle of delithiation, which is therefore a gradual process and is irreversible. It would be expected that, following extensive cycling and irrespective of either a charged or discharged state, the SEI will similarly mingle with Si. To verify this, we map the signature elements of the SEI at the charged state on the sample following 100 cycles (Supplementary Fig. 12), revealing that the SEI is indeed similarly mixed with Si as it is in the case of the discharged state. Moreover, the details of the SEI evolution in correlation with Li_xSi and the native SiO_x at the first cycle indeed show the nature of how a SEI in close contact with Si looks, which has been well addressed in a recent publication[25]. Therefore, it would be expected that even gradual SEI growth towards the interior of Si would lead to a mingled structure of Si with the SEI, while the SEI on each Si domain is likely similar to what has been observed for the case of the first cycle.

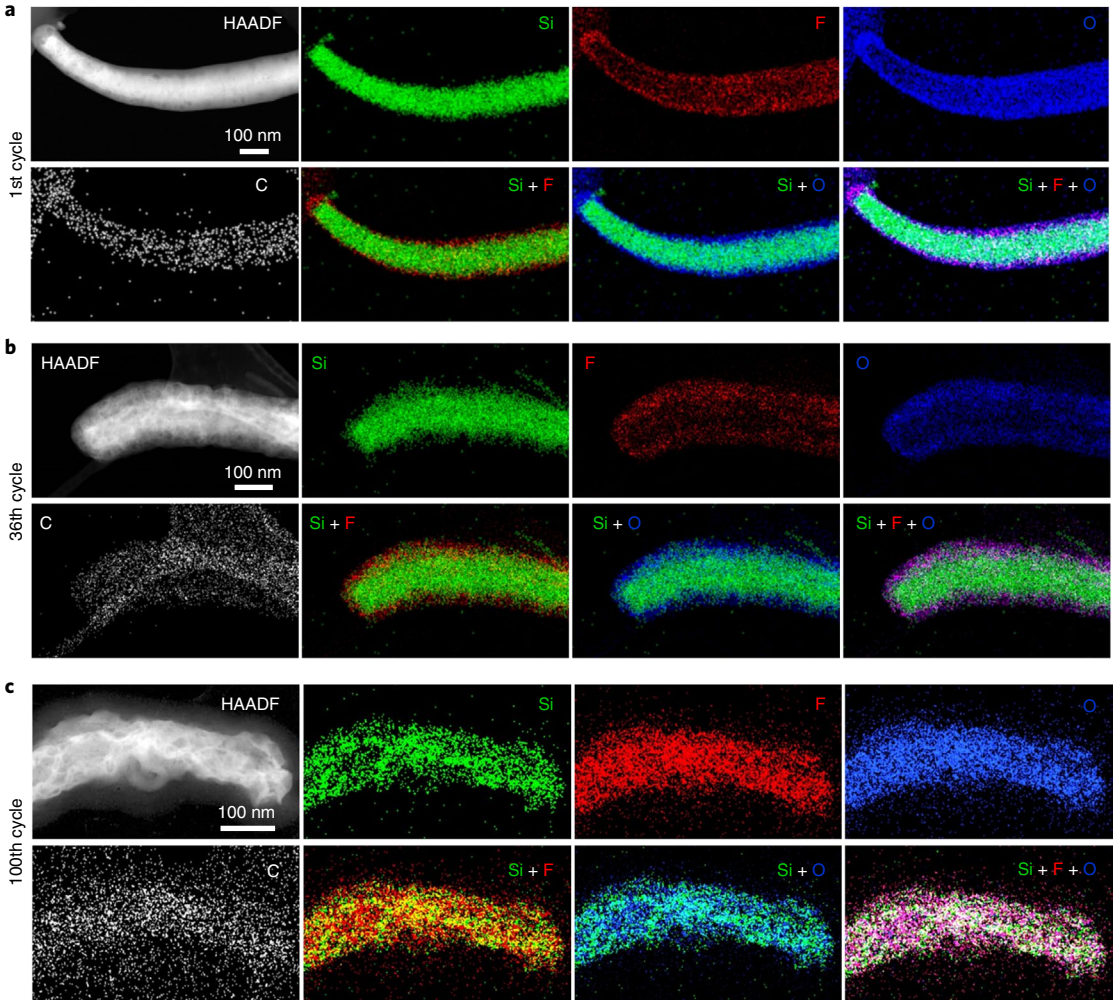

Fig. 2 | Cryo-STEM-HAADF image and EDS elemental composition mapping to illustrate the structural and chemical evolution of Si and the SEI upon cycling. a, Upon the first cycling, the Si–SEI is spatially correlated as the classic model of core–shell structure. **b**,**c**, After the 36th (**b**) and 100th (**c**) cycles, morphologically, the original Si nanowire gradually becomes irregular. Spatially, the Si and SEI no longer appear as a clearly defined core–shell structure after the 100th cycle; the Si and SEI are mixed to form a composite structure that resembles a plum pudding. Note that the mapping data are extracted from the title series of the EDS tomography experiments, and the nanowires for each of the different cycles are different samples, showing a representative case following each cycling condition. The image resolution is 512 × 512 pixels. The pixel sizes for the maps in **a**, **b** and **c** are 2.134 nm, 1.48 nm and 1.068 nm, respectively. The Gaussian blur filter (kernel size, 0.8) was applied to the maps to make the elements more visible.

Factors contributing to Si capacity loss. The gradual growth of the SEI towards the interior of the Si can directly result in capacity loss. First, it disrupts the electron and Li^+ ion conduction pathways within the porous core, increasing impedance and rendering capacity loss at a constant discharging rate and cut-off voltage. The capacity loss from the increased impedance within the core can be partially recovered by using a lower discharge current (Supplementary Fig. 2). Second, with increasing segmentation of the porous Si core by a chemomechanical effect[24,32,37,38] and vacancy accumulation, the SEI's inward growth can engulf and insulate the Si domains (Fig. 4c,f), depriving them from further electrochemical reactions. Note that the inhomogeneous electrochemical reactions within the Si core as a result of the SEI's inward growth is expected to exacerbate the chemomechanical effect[38], driving the continuous segmentation of the Si core and hence prompting the inward growth of the SEI. The integrity of the Si core after 36 cycles has not been obviously damaged (Supplementary Videos 3 and 4), meaning that the volume fraction of the engulfed and insulated Si is not substantial and hence the capacity loss is low (5.5%; Fig. 1e). By contrast, after 100 cycles, the Si nanowire core is severely segmented and overwhelmed by the SEI (Supplementary Videos 5 and 6), which is consistent with the observed obvious capacity loss (30.8%; Fig. 1e).

Moreover, the SEI growth towards the interior of the Si prompts the oxidation of Si, lowering the capacity of Si, which is supported by the electronic structural evolution of Si with progressive cycling. We capture electron energy loss spectroscopy (EELS) images of the Si L edge at the surface and at the core following the 1st, 36th and 100th cycles, and these EELS images are compared with standard EELS images of the Si L edge of Si and SiO_2, as shown in Supplementary Fig. 13. We find that the EELS fine structure features at the core and the surface of the Si nanowire gradually evolve with cycling. Following the first cycle, the surface layer shows no Si, indicating a SEI. With progressive cycling to the 36th cycle, the core is still dominated by the Si feature (note, this is a core–shell feature), while the surface shows increased features of silicon oxide. After the 100th delithiation, the silicon oxide contribution is enhanced, in contrast with that of the 36th cycle; this is especially true for the case of the surface (Supplementary Fig. 13). These gradual oxidation features cannot be attributed to the native oxide layer on the pristine Si nanowire (Supplementary Fig. 14). The behaviour of the

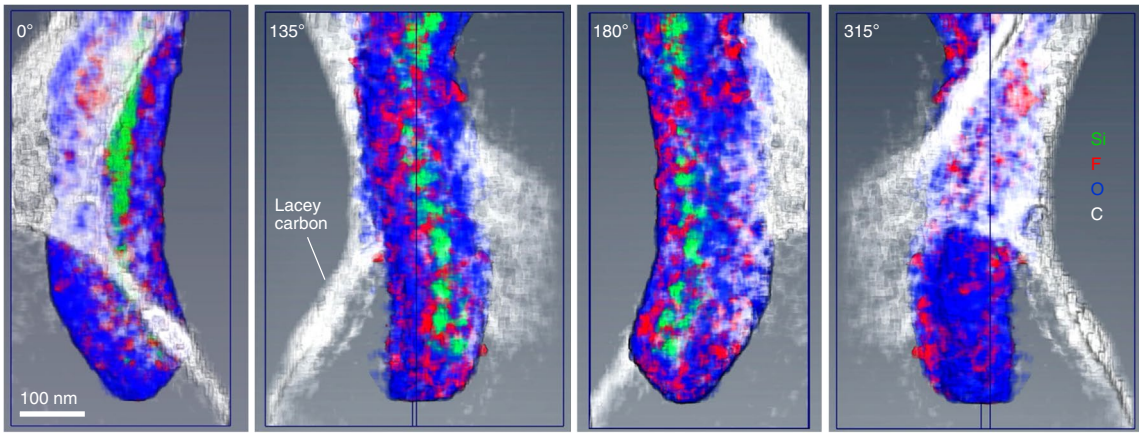

Fig. 3 | Cryo-STEM-EDS tomography on 3D structure and elemental distribution of the Si–SEI composite after 36 cycles. The degree values on each snapshot indicate the viewing angles of the snapshots.

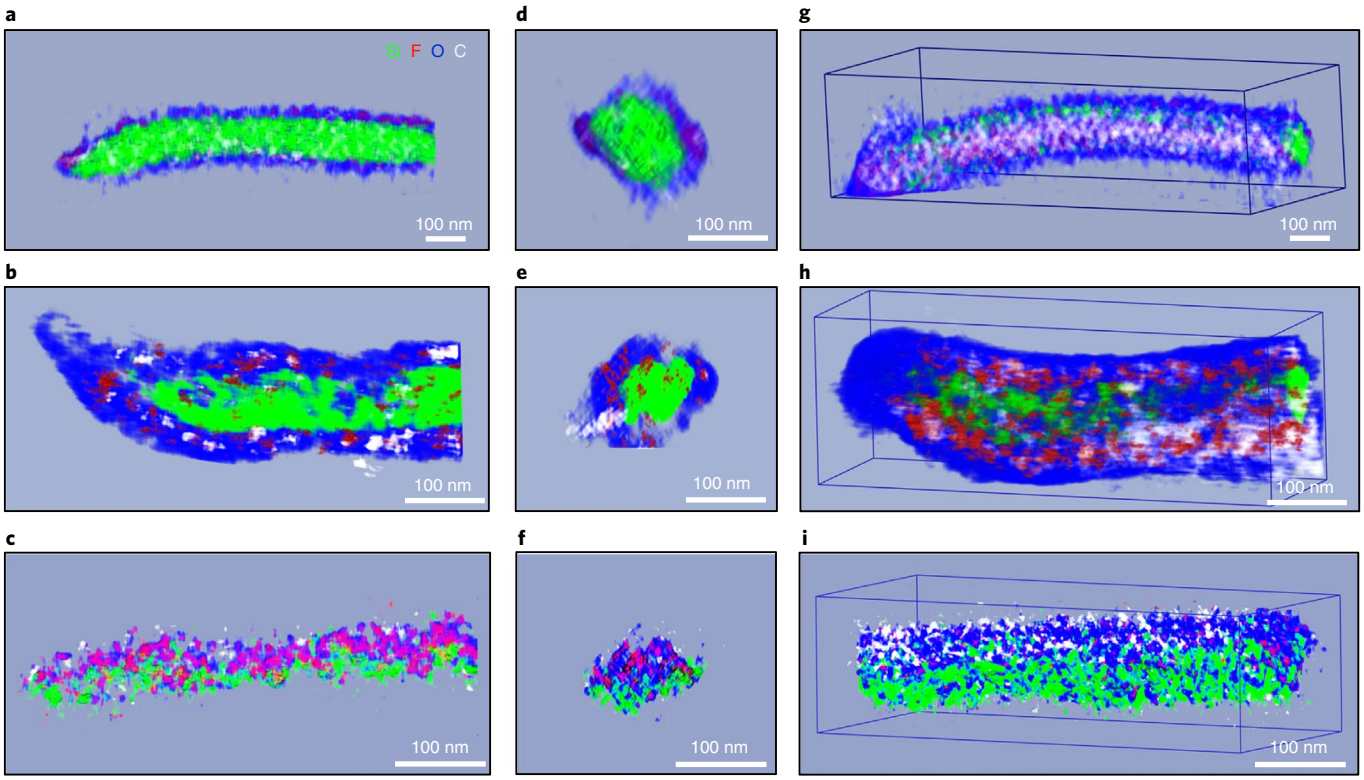

Fig. 4 | Segmented viewing of 3D cryo-STEM-EDS chemical composition from two directions to illustrate the spatially correlated evolution of the Si and SEI layer with battery cycles. a–c, Segmented view parallel to the wire axis after the 1st cycle (**a**), 36th cycle (**b**) and 100th cycle (**c**). Slice thickness is 5 nm. Each element is colour coded. **d–f**, Segmented cross-section view for the 1st (**d**), 36th (**e**) and 100th (**f**) cycles, revealing the SEI inward growth, gradual engulfing of Si by the SEI and attendant evolution of the core–shell structure to the plum-pudding structure. Slice thickness is 5 nm. **g–i**, The 3D view for the 1st (**g**), 36th (**h**) and 100th (**i**) cycles.

native silicon oxide upon initial cycling has been well documented in a recent publication[25]. Apparently, with the gradual permeation of the electrolyte into the Si core during cycling, it is reasonable to expect that dangling bonds on the Si surface upon delithiation can bond with oxygen in the electrolyte to lead to the gradual oxidation of Si as demonstrated by the EELS results.

Role of vacancy formation and condensation on Si–SEI evolution. To further appreciate the underlying mechanism of the growth of the SEI towards the interior of the Si, we developed a phase field model to simulate the morphological evolution of the silicon nanowires under electrochemical cycling. As detailed in the Methods, the model simultaneously tracks the large deformation induced by Li insertion and extraction; vacancy formation and condensation into voids; and SEI formation through the percolation diffusion channels during cycling. Our simulations reveal the intriguing mechanism of inward SEI growth, as shown by the cross-sectional views in Fig. 5a–f. Starting from an intact Si

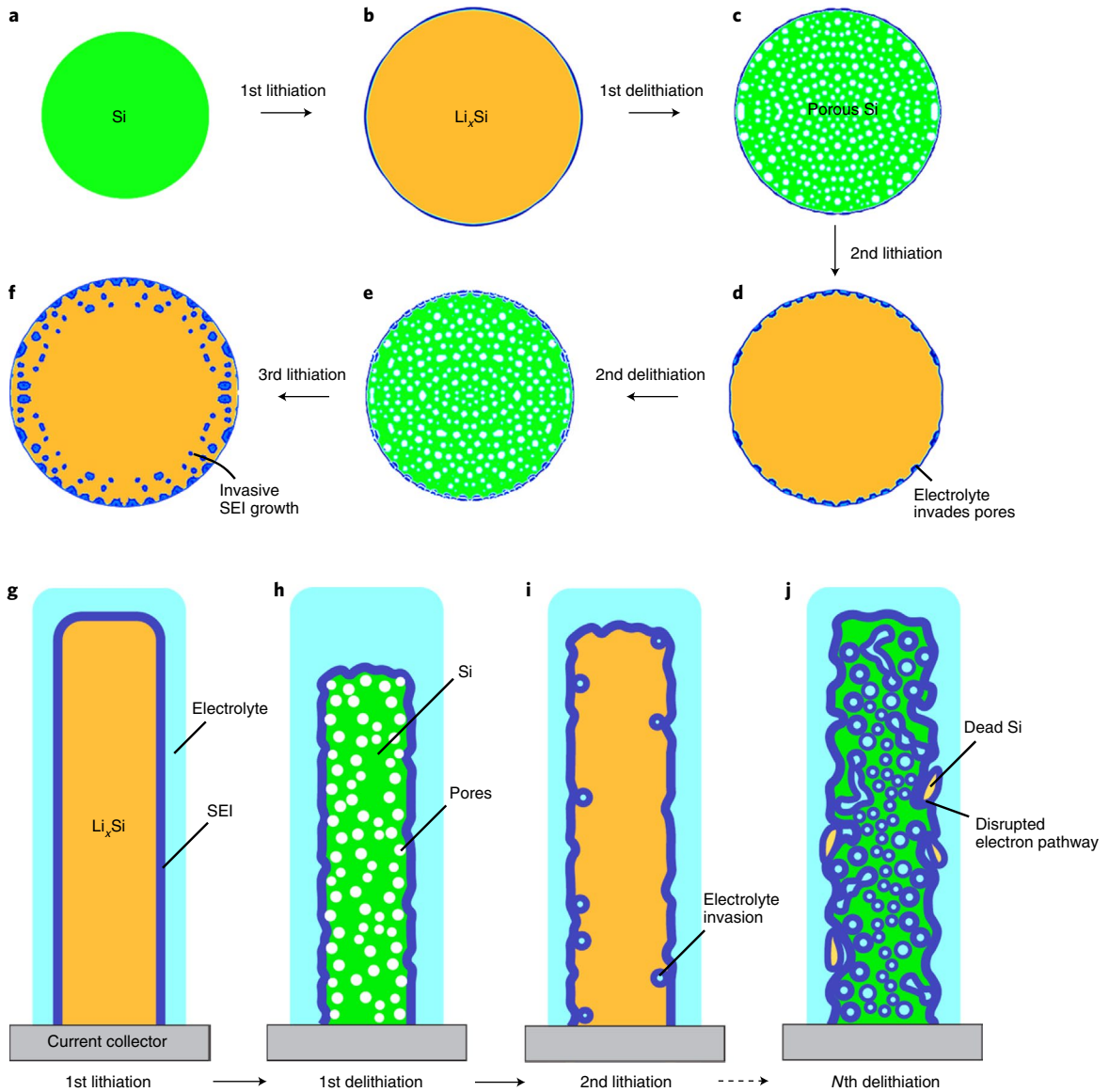

Fig. 5 | Microstructure-based modelling of the SEI inward growth during lithiation/delithiation cycles. a, A slice of silicon nanowire in the intact configuration. **b**, First lithiation generates large volume expansion and SEI formation at the outer surface. **c**, Void nucleation during the first delithiation. **d**, Liquid electrolytes percolate into the voids proximal to the outer surface of the nanowire, forming a SEI layer on the void surface, while other voids inaccessible to liquid electrolytes are annihilated during the second lithiation. **e**, The voids accessible to the liquid electrolytes are preserved and enlarged during the second delithiation. **f**, The liquid electrolytes invade, and concomitantly the SEI grows further into the nanowire core during the third lithiation. **g**–**j**, Schematic illustration of the capacity fading mechanism of nanosized Si in a liquid cell. The first lithiation generates large volume expansion and formation of a SEI at the outer surface (**g**). Voids nucleate during the first delithiation (**h**). During the second lithiation, liquid electrolytes percolate into the voids proximal to the outer surface of the nanowire, forming a SEI layer on the void surface (**i**). In contrast to other voids inaccessible to liquid electrolytes, these voids are not annihilated during further lithiation. After many cycles (**j**), liquid electrolytes and SEI growth penetrate deeper into the Si nanowire core, leading to a sponge-like structure, obstruction of the electron conduction pathways therein and dead Li domains. Green, Si; yellow, Li_xSi; blue, SEI; white, voids; turquoise, electrolyte.

nanowire (Fig. 5a), Li insertion during the first cycle causes large swelling and formation of a SEI layer at the nanowire's outer surface (Fig. 5b). During the first delithiation, Li vacancy condensation leads to the nucleation and growth of distributed voids in the nanowire (Fig. 5c). This directly explains the experimental observations in Fig. 1g and Supplementary Fig. 15. Noticeably, voids proximal to the outer surface of the nanowire form continuous channels and become accessible to the liquid electrolytes. Thus, during the second cycle, the liquid electrolyte percolates into these voids and at the same time forms a SEI layer on the internal surface of the voids (Fig. 5d,e). These liquid-electrolyte-filled and SEI-lining voids are preserved during further lithiation, while the voids that are further inside the core and inaccessible to the liquid electrolytes are annihilated due to the lithiation-induced deformation and mass flow (Fig. 5f). Upon subsequent delithiation cycles, new voids are nucleated in the close vicinity of the preserved voids in the previous cycles, densifying and enlarging the voids, and extending the percolation channels further into the Si nanowire. Meanwhile, the voids nucleated at the core of the nanowire remain uniform at a smaller size. The extended percolation channels facilitate further electrolyte invasion and SEI formation in the next lithiation cycle. This process repeats with the electrochemical cycles, and the liquid electrolytes

invade progressively into the core of the nanowire, leading to the experimentally observed plum-pudding morphology (as schematically illustrated in Fig. 5g–j).

The consistent observation and modelling described above lead to a pictorial description of the spatially coupled evolution of Si and SEI, offering a clear mechanistic understanding on the factor (beyond being the consequence of the volume change of Si, as perceived in the literature) that causes the capacity fading of Si. The structure starts with Si covered with a SEI shell. As the electrolyte permeates along the percolation channels formed by the evolving voids during the lithiation/delithiation cycles[39], the SEI forms on the surface of the voids and progressively grows inward. Through chemomechanical effects[38], the unique growth mode of the SEI can further exacerbate the structural degradation of the Si nanowire[40]. With increasing structural deterioration of the Si core, the SEI gradually engulfs the segmented Si domain within the Si core, disrupting electron conduction pathways, depriving the engulfed Si domains of electrochemical reactions and hence resulting in capacity loss. Li trapping has been perceived to contribute to the capacity loss[41]. Our present observation is fully consistent with the fading associated with Li trapping. In fact, the fading mode related to Li trapping can be subsumed into our findings. As shown in Supplementary Fig. 16, with progressive cycling, the SEI grown towards the interior of the Si itself holds Li. Furthermore, if the Si domains contain Li at the moment of complete loss of contact, the Li therein will be trapped. In this sense, the 'Li trapping' is a consequence of the presented mode of fading. To make sure the Li trapping is not associated with the liquid electrolyte trapping in the pore during sample preparation, we carried out EELS analysis of the pore region, in contrast with that of frozen liquid electrolyte (Supplementary Fig. 17). The engulfed Si domains could be detached from the nanowire following the removal of the SEI, resulting in the apparent loss of active Si as reported in a previous study[23]. The concurrent evolution of Si and growth of the SEI towards the Si interior are likely not the only capacity fading mechanism in nanosized Si; the extended SEI, as has been discovered on Li metal[42] and graphite[43] anodes, may exist on Si and contributes to the fading of Si.

Apparently, what we observed here is the consequence of a vacancy-condensation-mediated process, which, irrespective of the size of Si or the species of electrolyte, will naturally happen as long as Si is in direct contact with the liquid electrolyte upon battery cycling. As such, for the case of the Si nanowire using electrolyte without fluoroethylene carbonate additive, following the 36th cycle, the SEI has been noticed to grow towards the interior of the Si (Supplementary Figs. 18 and 19). In this sense, for a porous-structure Si, a nanosized Si domain will similarly be subjected to the gradual growth of the SEI towards the interior of the Si. It is this process that accounts for why with extended cycling, the nanosized Si becomes jagged, as widely noticed in the published literature[3,20,24]. Therefore, the present observation does not contradict what has been reported previously regarding porous-structured Si; instead, it reveals another level of factor causing fading, which is intrinsically related to vacancy generation and condensation during cycling. The structure and chemical composition of the SEI layer should also affect the degree of the SEI's inward growth, Li transport throughout the nanowire and hence the capacity retention. Apparently, more work needs to be done along this direction. Overall, if a stable or strong SEI is formed to prevent liquid electrolyte from contacting the Si, then the process of vacancy-condensation-mediated SEI growth towards the interior of Si can be mitigated.

Implications for Si anode design. In terms of material design, though the porous-structured Si can mitigate the pulverization of the Si and volume expansion of the anode[8,11,44], without an appropriate coating for isolating the Si from contacting the liquid electrolyte, the Si will still suffer from the fading mechanism, as demonstrated above. The mechanism clearly indicates that encapsulating Si with robust ionic and electronic conductive materials can be very effective in mitigating the capacity fading of the materials, which essentially has been well and consistently demonstrated in previous, ingenious, material-design concepts, such as the yolk–shell structure[10], pomegranate-mimic structure[7], graphene[6,11] and self-healing polymer enclosures[45]. In-situ formation of a hard-shell SEI will also similarly mitigate the fading factor, as identified here[1]. Recently, on Battery Day, Tesla announced targeting to use mined, large Si with a coating layer for the anode in their car battery. The present article's revelations, in combination with previously reported nanoscale design concepts, indicate a coating approach that is technologically on track for solving the Si problem.

Conclusions

In stark contrast to the relatively stable SEI on graphite, the instability of the SEI on Si, as manifested by the growth of this SEI towards the interior of the Si and the formation of dead Si, originates in the continuous development of voids and the permeation of liquid electrolyte along the percolated void channel with cycling. The present work shows the critical role of vacancies left behind by the working Li ions, rather than the instability being a mere response of the SEI to the volume swing of the electrode. Since void nucleation and growth, coupled with the large volume swing, are ubiquitous for all the alloying-type anodes including Li metal, the SEI evolution model established here should be generally applicable to these anodes. In a broader view, active materials that are subject to structural deteriorations, for example, cathode particle aggregates[46] that can lead to electrolyte permeation, should all experience such a failure mechanism. The mechanistic understanding points to restraining electrolyte permeation as a key strategy to enable the stable cycling and high-capacity retention of active electrode materials in lithium-ion batteries.

Online content

Any methods, additional references, Nature Research reporting summaries, source data, extended data, supplementary information, acknowledgements, peer review information; details of author contributions and competing interests; and statements of data and code availability are available at https://doi.org/10.1038/s41565-021-00947-8.

Received: 12 August 2020; Accepted: 16 June 2021;
Published online: 29 July 2021

References

1. Chen, J. et al. Electrolyte design for LiF-rich solid–electrolyte interfaces to enable high-performance microsized alloy anodes for batteries. *Nat. Energy* **5**, 386–397 (2020).
2. Wu, H. et al. Stable cycling of double-walled silicon nanotube battery anodes through solid–electrolyte interphase control. *Nat. Nanotechnol.* **7**, 310–315 (2012).
3. Chan, C. K. et al. High-performance lithium battery anodes using silicon nanowires. *Nat. Nanotechnol.* **3**, 31–35 (2008).
4. Kim, H., Lee, E.-J. & Sun, Y.-K. Recent advances in the Si-based nanocomposite materials as high capacity anode materials for lithium ion batteries. *Mater. Today* **17**, 285–297 (2014).
5. Choi, S., Kwon, T. W., Coskun, A. & Choi, J. W. Highly elastic binders integrating polyrotaxanes for silicon microparticle anodes in lithium ion batteries. *Science* **357**, 279–283 (2017).
6. Li, Y. et al. Growth of conformal graphene cages on micrometre-sized silicon particles as stable battery anodes. *Nat. Energy* **1**, 15029 (2016).
7. Liu, N. et al. A pomegranate-inspired nanoscale design for large-volume-change lithium battery anodes. *Nat. Nanotechnol.* **9**, 187–192 (2014).
8. An, W. et al. Scalable synthesis of ant-nest-like bulk porous silicon for high-performance lithium-ion battery anodes. *Nat. Commun.* **10**, 1447 (2019).
9. Magansinski, A. et al. High-performance lithium-ion anodes using a hierarchical bottom-up approach. *Nat. Mater.* **9**, 353–358 (2010).

10. Liu, N. et al. A yolk-shell design for stabilized and scalable Li-ion battery alloy anodes. *Nano Lett.* **12**, 3315–3321 (2012).
11. Lu, Z. et al. Nonfilling carbon coating of porous silicon micrometer-sized particles for high-performance lithium battery anodes. *ACS Nano* **9**, 2540–2547 (2015).
12. Szczech, J. R. & Jin, S. Nanostructured silicon for high capacity lithium battery anodes. *Energy Environ. Sci.* **4**, 56–72 (2011).
13. Huang, S., Fan, F., Li, J., Zhang, S. & Zhu, T. Stress generation during lithiation of high-capacity electrode particles in lithium ion batteries. *Acta Mater.* **61**, 4354–4364 (2013).
14. Kim, H., Han, B., Choo, J. & Cho, J. Three-dimensional porous silicon particles for use in high-performance lithium secondary batteries. *Angew. Chem. Int. Ed.* **47**, 10151–10154 (2008).
15. Kennedy, T., Brandon, M. & Ryan, K. M. Advances in the application of silicon and germanium nanowires for high-performance lithium-ion batteries. *Adv. Mater.* **28**, 5696–5704 (2016).
16. Liu, X. H. et al. Size-dependent fracture of silicon nanoparticles during lithiation. *ACS Nano* **6**, 1522–1531 (2011).
17. Zhao, K. et al. Concurrent reaction and plasticity during initial lithiation of crystalline silicon in lithium-ion batteries. *J. Electrochem. Soc.* **159**, A238–A243 (2012).
18. Gohier, A. et al. High-rate capability silicon decorated vertically aligned carbon nanotubes for Li-ion batteries. *Adv. Mater.* **24**, 2592–2597 (2012).
19. Yoon, T., Nguyen, C. C., Seo, D. M. & Lucht, B. L. Capacity fading mechanisms of silicon nanoparticle negative electrodes for lithium ion batteries. *J. Electrochem. Soc.* **162**, A2325–A2330 (2015).
20. Wetjen, M. et al. Morphological changes of silicon nanoparticles and the influence of cutoff potentials in silicon-graphite electrodes. *J. Electrochem. Soc.* **165**, A1503–A1514 (2018).
21. Chan, C. K., Ruffo, R., Hong, S. S. & Cui, Y. Surface chemistry and morphology of the solid electrolyte interphase on silicon nanowire lithium-ion battery anodes. *J. Power Sources* **189**, 1132–1140 (2009).
22. Krause, L. J., Brandt, T., Chevrier, V. L. & Jensen, L. D. Surface area increase of silicon alloys in Li-ion full cells measured by isothermal heat flow calorimetry. *J. Electrochem. Soc.* **164**, A2277–A2282 (2017).
23. Cho, J. H. & Picraux, S. T. Silicon nanowire degradation and stablization during lithium cycling by SEI layer formation. *Nano Lett.* **14**, 3088–3095 (2014).
24. Zhang, Q. et al. Harnessing the concurrent reaction dynamics in active Si and Ge to achieve high performance lithium-ion batteries. *Energy Environ. Sci.* **11**, 669–681 (2018).
25. Huang, W. et al. Dynamic structure and chemistry of the silicon solid-electrolyte interphase visualized by cryogenic electron microscopy. *Matter* **1**, 1232–1245 (2019).
26. Midgley, P. A. & Dunin-Borkowski, R. E. Electron tomography and holography in materials science. *Nat. Mater.* **8**, 271–280 (2009).
27. Zhou, J. et al. Observing crystal nucleation in four dimensions using atomic electron tomography. *Nature* **570**, 500–503 (2019).
28. Turoňová, B. et al. Benchmarking tomographic acquisition schemes for high-resolution structural biology. *Nat. Commun.* **11**, 876 (2020).
29. Li, Y. et al. Atomic structure of sensitive battery materials and interfaces revealed by cryo-electron microscopy. *Science* **358**, 506–510 (2017).
30. Wang, X. et al. New insights on the structure of electrochemically deposited lithium metal and its solid electrolyte interphases via cryogenic TEM. *Nano Lett.* **17**, 7606–7612 (2017).
31. Liu, X. H. et al. Anisotropic swelling and fracture of silicon nanowires during lithiation. *Nano Lett.* **11**, 3312–3318 (2011).
32. Choi, J. W. et al. Stepwise nanopore evolution in one-dimensional nanostructures. *Nano Lett.* **10**, 1409–1413 (2010).
33. Chen, Q. & Sieradzki, K. Spontaneous evolution of bicontinuous nanostructures in dealloyed Li-based systems. *Nat. Mater.* **12**, 1102–1106 (2013).
34. Hu, Y. S. et al. Electrochemical lithiation synthesis of nanoporous materials with superior catalytic and capacitive activity. *Nat. Mater.* **5**, 713–717 (2006).
35. Wang, A., Kadam, S., Li, H., Shi, S. & Qi, Y. Review on modeling of the anode solid electrolyte interphase (SEI) for lithium-ion batteries. *npj Comput. Mater.* **4**, 15 (2018).
36. Ploehn, H. J., Ramadass, P. & White, R. E. Solvent diffusion model for aging of lithium-ion battery cells. *J. Electrochem. Soc.* **151**, A456–A462 (2004).
37. Pharr, M., Zhao, K., Wang, X., Suo, Z. & Vlassak, J. J. Kinetics of initial lithiation of crystalline silicon electrodes of lithium-ion batteries. *Nano Lett.* **12**, 5039–5047 (2012).
38. Zhang, S. Chemomechanical modeling of lithiation-induced failure in high-volume-change electrode materials for lithium ion batteries. *npj Comput. Mater.* **3**, 7 (2017).
39. Zhu, J. et al. In situ TEM of phosphorus-dopant-induced nanopore formation in delithiated silicon nanowires. *ACS Appl. Mater. Interfaces* **11**, 17313–18320 (2019).
40. Chen, C. et al. Impact of dual-layer solid-electrolyte interphase inhomogeneities on early-stage defect formation in Si electrodes. *Nat. Commun.* **11**, 3283 (2020).
41. Zhu, B. et al. Minimized lithium trapping by isovalent isomorphism for high initial Coulombic efficiency of silicon anodes. *Sci. Adv.* **5**, eaax0651 (2019).
42. Zachman, M. J., Tu, Z., Choudhury, S., Archer, L. A. & Kourkoutis, L. F. Cryo-STEM mapping of solid–liquid interfaces and dendrites in lithium-metal batteries. *Nature* **560**, 345–349 (2018).
43. Huang, W. et al. Evolution of the solid–electrolyte interphase on carbonaceous anodes visualized by atomic-resolution cryogenic electron microscopy. *Nano Lett.* **19**, 5140–5148 (2019).
44. Xiao, Q. et al. Inward lithium-ion breathing of hierarchically porous silicon anodes. *Nat. Commun.* **6**, 8844 (2015).
45. Wang, C. et al. Self-healing chemistry enables the stable operation of silicon microparticle anodes for high-energy lithium-ion batteries. *Nat. Chem.* **5**, 1042–1048 (2013).
46. Yan, P. et al. Tailoring grain boundary structures and chemistry of Ni-rich layered cathodes for enhanced cycle stability of lithium-ion batteries. *Nat. Energy* **3**, 600–605 (2018).

Methods

Cell assembly and electrochemical test. Electrochemical experiments were performed using CR2016-type coin cells with Celgard3501 as the separator and lithium foil as the counter-electrode. The electrolyte was 1.2 M $LiPF_6$ in a mixture of ethylene carbonate and dimethyl carbonate (3:7 by weight), plus 10 wt% fluoroethylene carbonate. The working electrode was silicon nanowire directly grown on the stainless steel. The coin cells were assembled in an Ar-filled glove box with O_2 and H_2O levels <0.1 ppm. The electrochemical performances were evaluated on a LAND battery tester at 25 °C. The cut-off voltage was 0.02 V versus Li/Li^+ for lithiation and 1.5 V for delithiation. The cell was cycled once at 0.06 mA cm^{-2} current density (~0.1 C rate) for formation and then cycled at 0.4 mA cm^{-2} current density (~1 C rate) for the subsequent cycles. The capacity retention was calculated based on the specific delithiation capacity of the second cycle.

TEM sample preparation. The coin cells were disassembled directly inside an Ar-filled glove box. The working electrode was rinsed three times using dimethyl carbonate to remove residual electrolyte and then dried in vacuum for ~15 min. Then, a lacey carbon Cu mesh TEM grid was placed on top of the working electrode and gently pressed on the electrode to pick up the nanowires. Since our anodes are free of binder and conductive substances, the materials picked up from the anode should be only the Si nanowire and the SEI. Then, the TEM grid was cooled sufficiently in liquid nitrogen under Ar gas protection, loaded onto a precooled cryo-TEM holder (Gatan Elsa), and quickly inserted into the TEM chamber. The total exposure time of the sample to the air was ~10 s at approximately −170 °C. The reaction between the sample and air was thereby minimized, preserving the material in the 'as-cycled' state for the TEM characterization.

Cryo-STEM-EDS tomography. The cryo-STEM-EDS tomography of the cycled samples was performed on a Talos F200X STEM instrument equipped with four SuperX EDS detectors. The EDS maps were collected using Velox software (Thermo Fisher Scientific). The tomography tilt series were acquired using Thermo Fisher Scientific's tomography acquisition software. The functions of auto-eucentric height, auto-tracking, auto-focus, auto-tilt, auto-acquiring, auto-store, drift correction and low dose acquisition mode were utilized for acquiring the tomography datasets (details in Supplementary Figs. 22 and 23). A tilt series was acquired from +60° to −60° at an increment of 5°, under a 200 kV, ~150–250 pA electron beam, at a dwell time of 40 µs or 20 µs. The sample temperature was maintained at approximately −178 °C during the whole process. The total tomography acquisition time was ~1.5 h, including a total EDS mapping time of ~45 min. These parameters enable us to capture the spatial distribution of the SEI without inducing severe damage to the sample, as determined by comparing the STEM images of the Si nanowire before and after the acquisition. Note that pores were identified within the SEI and on the SEI–Si interface that, other than beam damage, can be attributed to the outward diffusion of the vacancies from the Si core and/or gas formation from the solid–electrolyte reactions. A detailed evaluation of the electron beam effect and optimization of imaging conditions is discussed in the Supplementary Information with Supplementary Figs. 20–30. The Kα peaks of O, F, Si and C were used for generating maps with the background subtracted. The background is subtracted using a multi-polynomial model fitting for background correction as discussed in the Supplementary Information with Supplementary Fig. 31. To further illustrate the quality of the EDS, we also show the EDS spectrum at 1×1 pixel (Supplementary Figs. 32–36) and 5×5 pixels (Supplementary Fig. 37).

The Inspect 3D software (Thermo Fisher Scientific) was used to align and reconstruct the data of the tilt series to a 3D volume. For the tomography data processing, the resolution of the input maps was 512×512 pixels with the pixel size for the maps of the 1st, 36th and 100th cycled Si nanowires being 2.134 nm, 1.48 nm and 1.068 nm, respectively. No smoothing filter was used for the input maps. The expectation–maximization algorithm in Thermo Fishers Scientific's Inspect 3D was used as the reconstruction algorithm. In statistics, the expectation–maximization algorithm is an iterative method to find (local) maximum likelihood or maximum a posteriori estimates of parameters in statistical models, where the model depends on unobserved latent variables[47]. Expectation–maximization is more or less like simultaneous iterative reconstruction technique and is actually also known as multiplicative simultaneous iterative reconstruction technique (as opposed to additive simultaneous iterative reconstruction technique)[47]. The advantage of using expectation–maximization is that it reduces the elongation of particles and dampens more missing wedge artefacts, as shown in Supplementary Fig. 29. Within Inspect 3D, the ASTRA toolbox was utilized for the reconstruction[48]. The number of the expectation–maximization reconstruction iterations was 20. The Avizo 3D software (Thermo Fisher Scientific) was utilized to create volume renderings of the reconstructed 3D volume for different elements and HAADF, and to align them together to create a mixture of 3D element maps. Segmentation was done with Avizo 3D to remove the carbon substrates from the Si nanowire after the 36th cycle. The carbon substrates can be easily differentiated from the carbon within the SEI on the Si nanowire from certain viewing angles in Avizo 3D.

The Gaussian filter is a kernel-based blurring filter, which redistributes the counts from a single pixel to an area of surrounding pixels with a factor that decreases as the distance increases. For the two-dimensional elemental maps shown in Fig. 2, the Gaussian blur filter with kernel size of 0.8 was used. The approximate resolution (minimum measurable feature size) of the 3D tomography was ~5 nm. As such, we unveiled the elemental distribution of the nanowire in three dimensions and then extracted the cross-sectional information therein.

STEM and EELS. STEM-HAADF and STEM-EELS were carried out using a Titan 80-300 (Thermo Fisher Scientific), which was fitted with a monochromator and probe forming a lens aberration corrector. The operating voltage was 300 kV. The STEM-EELS were carried out using a Gatan Image Filter (Quantum 965) that is post-column-attached to the Titan S/TEM instrument. The energy resolution of the EELS spectrometer was ~1.5 eV as measured by the full width at half magnitude of the zero-loss peak. The energy dispersion was 0.25 eV per channel. The typical dwell time for each pixel was ~0.1 ms for low loss and 10 ms for high loss. To minimize artefacts related to sample drift during the STEM–EELS mapping, the TEM sample was placed inside the TEM instrument for a few hours before the acquisition, and the mapping was drift corrected every 50 pixels. For the elemental mapping, the integration window was 50–80 eV for the Li K edge and 98–168 eV for the Si L edge.

Simulation of morphological evolution. To simulate the influence of the SEI on the morphological evolution of the silicon after charging/discharging cycles, we developed a phase field model on the cross-section of the silicon nanowire in experiments. Here we adopted the normalized lithium concentration, c_{Li}, to indicate the charging state of the silicon, where $c_{Li}=c_{max}$ indicates the fully charged state (as $Li_{3.75}Si$) and $c_{Li}=c_{min}$, the unlithiated or delithiated state of the electrode. Another field parameter, c_v, is also employed, as the concentration of the void, where $c_v=c_{min}$ denotes the Li_xSi phase and $c_v=c_{max}$, the vacancy phase generated during the charging/discharging cycles. The total chemical free energy can be described as

$$F = \int_V \left[f_{ch}(c_{Li}, c_v) + \tfrac{\kappa_{Li}}{2}(\nabla c_{Li})^2 + \tfrac{\kappa_v}{2}(\nabla c_v)^2 \right] dV \quad (1)$$

where $f_{ch}(c_{Li}, c_v)$ is the local chemical free energy; the second and third terms are the gradient energy of the lithium and void, respectively. Here κ_{Li} and κ_v are the coefficient associated with the surface energy of lithium and vacancy, respectively. V represents the volume. To be specific, the local chemical free energy is defined by the linear combination of two double-well functions to represent the local chemical free energy of the lithium and void, respectively, as[49]

$$f_{ch}(c_{Li}, c_v) = h(c_{Li}) f_{Li} + [1 - h(c_{Li})] f_v \quad (2)$$

where

$$f_{Li} = c_{max} RT[c_{Li} \ln c_{Li} + (1 - c_{Li}) \ln(1 - c_{Li}) + \Omega c_{Li}(1 - c_{Li})]$$

$$f_v = c_{max} RT[c_v \ln c_v + (1 - c_v) \ln(1 - c_v) + \Omega c_v (1 - c_v)] \quad (3)$$

Here $h(c_{Li})$ is an interpolating function where $h(c_{Li}=c_{max})=1$ and $h(c_{Li}=c_{min})=0$. R is the gas constant, T is the tempeature and Ω is a dimensionless parameter to control the profile of the double-well free energy functions.

Following the standard procedure of the phase field method, the kinetic equations governing the two-phase variables are[39]

$$\frac{\partial c_{Li}}{\partial t} = \nabla \cdot \left(M_{Li} \nabla \frac{\delta F}{\delta c_{Li}} \right) + S(\mathbf{x})(\nabla c_v)^2 \quad (4)$$

$$\frac{\partial c_v}{\partial t} = \nabla \cdot \left(M_v \nabla \frac{\delta F}{\delta c_v} \right) + R(\mathbf{x}) \frac{\partial c_{Li}}{\partial \mathbf{t}} \quad (5)$$

where the second term on the right side of equation (4) indicates the lithium flux on the newly generated surface in contact with the liquid electrolyte and $S(\mathbf{x})$ is the source function. Here M_{Li} and M_v are the mobilities of the lithium and vacancy, respectively, and $R(\mathbf{x})$ is a random source function for the nucleation of the vacancy at the reaction front.

To consider the volumetric changes induced by the lithium insertion/extraction, we take into account the elasto-plastic deformation in the Si electrode. The deformation for any infinitesimal volume element can be described by the deformation gradient tensor $\mathbf{F}(\mathbf{X}, t) = \partial \mathbf{x}/\partial \mathbf{X}$, where $\mathbf{x}$ is the position occupied by a material point in the current time t and $\mathbf{X}$ indicates its initial position. The gradient tensor can be expressed by the following multiplication decomposition as $\mathbf{F}=\mathbf{F}^e\mathbf{F}^c\mathbf{F}^p$, where the superscripts e, c and p indicate the elastic, chemical-induced and plastic gradient tensors, respectively. The total strain can be written as

$$\mathbf{E} = \tfrac{1}{2}(\mathbf{F}^T\mathbf{F} - \mathbf{I}) = (\mathbf{F}^c\mathbf{F}^p)^T\mathbf{E}^e\mathbf{F}^p\mathbf{F}^c + (\mathbf{F}^p)^T\mathbf{E}^c\mathbf{F}^p + \mathbf{E}^p \quad (6)$$

where $\mathbf{E}^{e} = \frac{1}{2}\left[(\mathbf{F}^{e})^{T}\mathbf{F}^{e} - \mathbf{I}\right]$, $\mathbf{E}^{c} = \frac{1}{2}\left[(\mathbf{F}^{c})^{T}\mathbf{F}^{c} - \mathbf{I}\right]$ and $\mathbf{E}^{p} = \frac{1}{2}\left[(\mathbf{F}^{p})^{T}\mathbf{F}^{p} - \mathbf{I}\right]$. Here the superscript T denotes the transpose of tensors and $\mathbf{I}$ is the identity tensor. The chemical deformation gradient, $\mathbf{F}^{c}$, can be written as $\mathbf{F}^{c} = (1 + \beta\frac{c_{Li} - c_{min}}{c_{max} - c_{min}})\mathbf{I}$, where β is the volumetric change coefficient. Then $\mathbf{F}^{e}$ and $\mathbf{F}^{p}$, as well as the stress tensor, can be obtained by solving the displacement field in the equilibrium equations. Here we use linear elasticity in the elastic region and the associated J_2-flow rule to describe the plastic yielding behaviour of the materials in the plastic region.

Note that two special treatments are adopted in our modelling. First, the SEI is not explicitly simulated in our model. Instead, we assume the liquid electrolyte increasingly diffuses into the Si nanowire through the voids that are proximal to the outer surface of the nanowire in a progressive manner in each cycle, where the SEI grows on the void surfaces that are accessible to the liquid electrolyte. Since the voids with the SEI on the surface are preserved, we assume a vanishing mobility (M_{Li}) within these voids during the lithiation. Second, vacancy condensation and void formation in Si is a gradual process over many cycles. Computationally it is very challenging to simulate these many cycles and show void formation. To overcome the computational complexity, we purposely shorten the time scale of the vacancy condensation by using a high mobility of vacancies and a large driving force for vacancy condensation. With this treatment, vacancy condensation and void formation can be computationally shown in the first few cycles. However, each cycle in our numerical simulation corresponds to tens of cycles in experiments. Also, these treatments do not invalidate the underlying mechanism of inward SEI growth revealed by the numerical simulations.

Our model is numerically implemented in the COMSOL Multiphysics package. The radius of the silicon nanowire, l_0, is 20 nm and the characteristic time step, $\Delta t = 1$ s. Other parameters used are listed in Supplementary Table 1. The charging/discharging cycles are achieved by setting different Dirichlet boundary conditions at the outside surface of the nanowire.

Data availability

All data that support the findings of this study have been included in the main text, Supplementary Information and Supplementary Videos 1–6. The original data are kept at the Environmental Molecular Sciences Laboratory at Pacific Northwest National Laboratory and are available from the corresponding authors upon request.

References

47. Sigworth, F. J., Doerschuk, P. C., Carazo, J.-M. & Scheres, S. H. W. An introduction to maximum-likelihood methods in cryo-EM. *Methods Enzymol.* **482**, 263–294 (2010).
48. Aarle, W. V. et al. The ASTRA Toolbox: a platform for advanced algorithm development in electron tomography. *Ultramicroscopy* **157**, 35–47 (2015).
49. Chen, L. et al. Modulation of dendritic patterns during electrodeposition: a nonlinear phase-field model. *J. Power Sources* **300**, 376–385 (2015).

Acknowledgements

This work was supported by the Assistant Secretary for Energy Efficiency and Renewable Energy, Office of Vehicle Technologies of the US Department of Energy. This work was performed partly at the William R. Wiley Environmental Molecular Sciences Laboratory, a national scientific user facility sponsored by the US Department of Energy, Office of Biological and Environmental Research and located at Pacific Northwest National Laboratory. Pacific Northwest National Laboratory is operated by Battelle for the US Department of Energy under contract DE-AC05-76RL01830. The cryo-STEM-EDS tomography was performed at the Hillsboro Nanoport of Thermo Fisher Scientific. We thank R. Warren for his assistance on the tomography data processing. This work was also performed, in part, at the Center for Integrated Nanotechnologies, an Office of Science User Facility operated for the US Department of Energy, Office of Science. S.Z. acknowledges support by the National Science Foundation (CBET-2034899).

Author contributions

C.W., J.-G.Z. and X.L. conceived the project. Y.H. and X.L. designed the experiment. J.Y. synthesized the Si nanowire on the stainless-steel anode. H.J. and R.Y. assembled and cycled the coin cells. Y.H. and Y.X. performed the cryo-TEM experiments. Y.H., L.J., A.G., and C.B.-M. conducted the cryo-STEM-EDS tomography experiments under the supervision of L.P. and T.T.; L.J. and M.S. conducted the tomography data reconstruction and visualization. T.C., D.X. and S.Z. carried out the modelling calculation. Y.H., L.J., C.W. and S.Z. draughted the manuscript. All authors contributed to the revision of the manuscript.

Competing interests

The authors declare no competing interests.

Additional information

Supplementary information The online version contains supplementary material available at https://doi.org/10.1038/s41565-021-00947-8.

Correspondence and requests for materials should be addressed to J.Y., X.L., S.Z. or C.W.

Peer review information *Nature Nanotechnology* thanks Peter Ercius and the other, anonymous, reviewer(s) for their contribution to the peer review of this work.

Reprints and permissions information is available at www.nature.com/reprints.

nature portfolio

https://doi.org/10.1038/s41565-021-00947-8

Supplementary information

Progressive growth of the solid–electrolyte interphase towards the Si anode interior causes capacity fading

In the format provided by the authors and unedited

Supplementary Information for

Solid-electrolyte interphase progressive growth towards the Si interior to cause capacity fading

Yang et al.

The Supplementary Information includes:

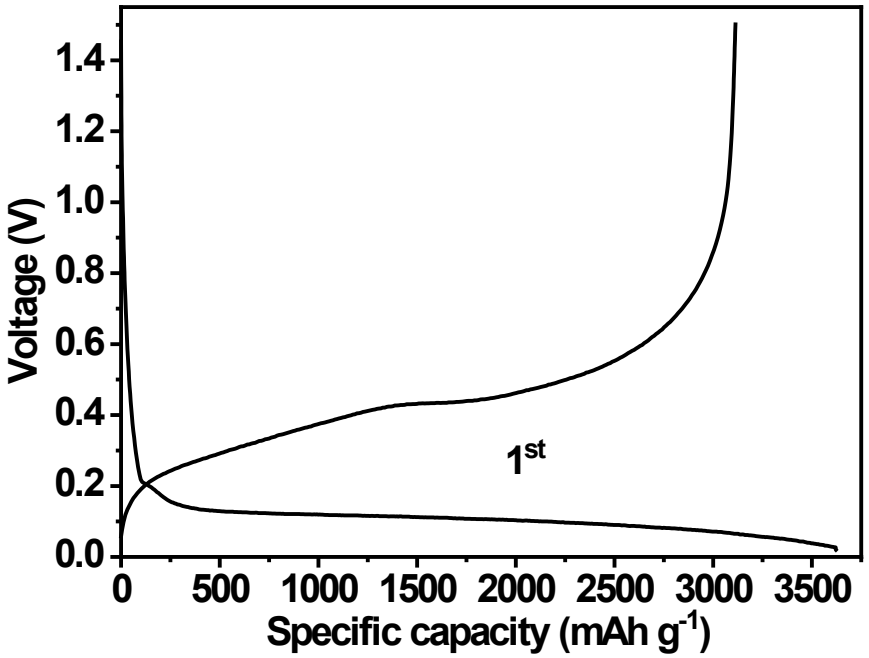

Supplementary Fig. 1 | Voltage profiles for the first galvanostatic cycles of the Si nanowires.

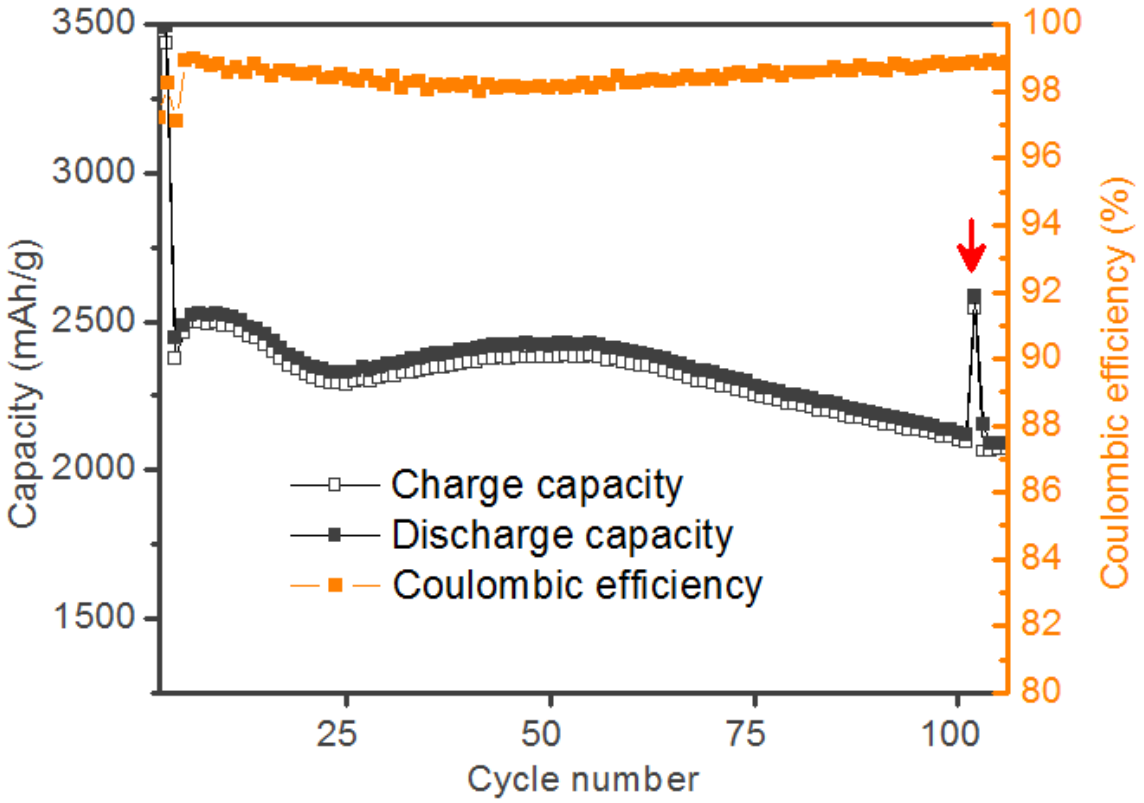

Supplementary Fig. 2 | Capacity and Coulombic efficiency evolution curves of another cell. We used 0.02C charge/discharge rate in the first two cycles and then cycled the nanowire at 1C for 98 cycles and then checked the capacity of the cell on the 101th cycle by using a much lower 0.02C discharge rate (as indicated by the red arrow). Clearly, the capacity loss from the increased impedance within the core is partly redeemed. Note that the capacity is averaged over total weight of the Si nanowires on the electrode.

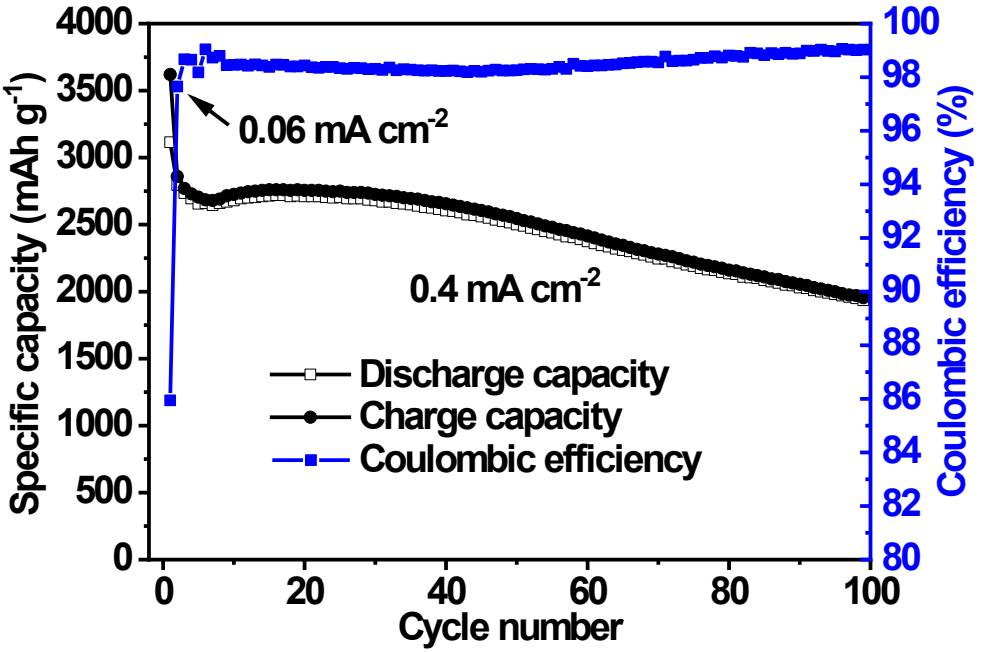

Supplementary Fig. 3 | Capacity and Coulombic efficiency as a function of cycle numbers for the Si nanowires.

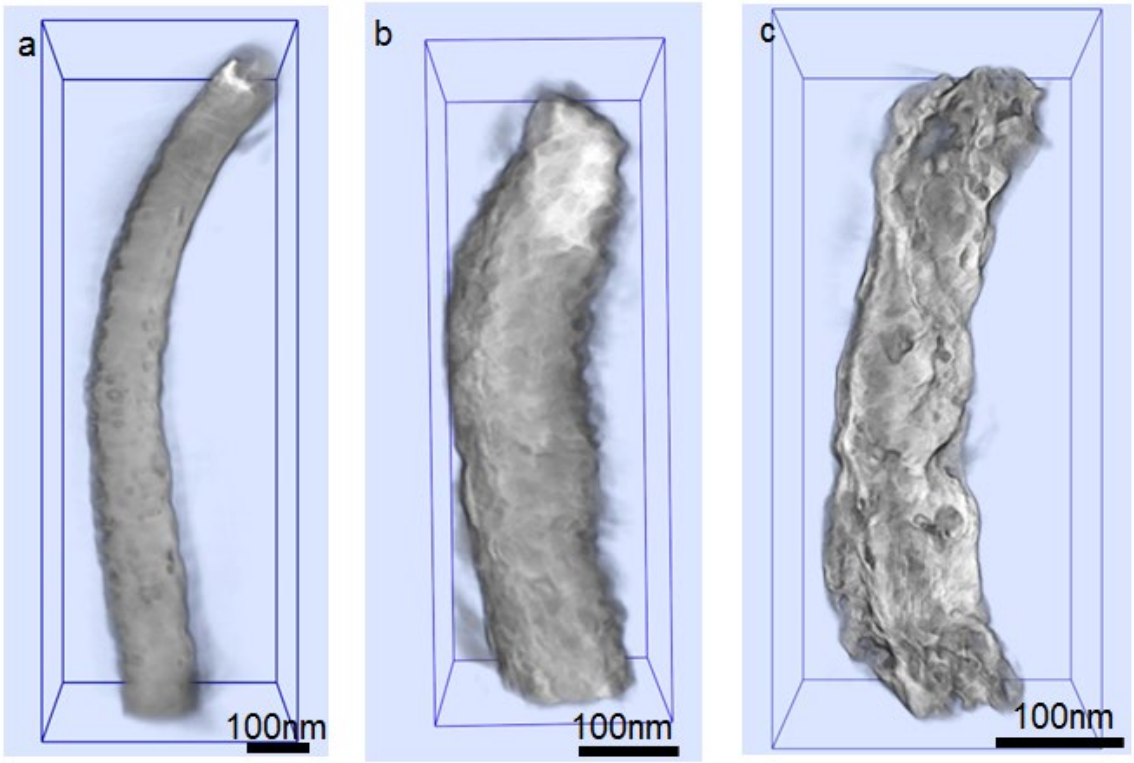

Supplementary Fig. 4 | Cryo-STEM HAADF tomography Si nanowires after 1st (a), 36th (b) and 100th cycles (c). Clearly, openings from surface to the interior of the nanowire gradually appeared after extensive cycling which can facilitate the permeation of the electrolyte molecules and hence inward growth of the SEI.

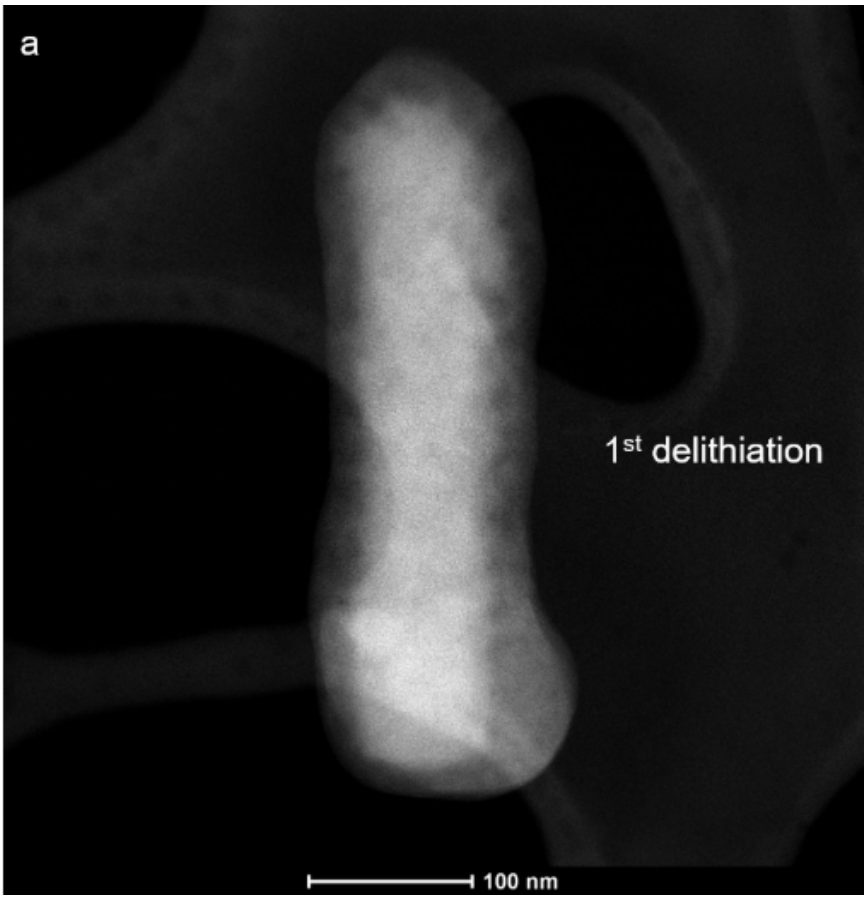
a
1st delithiation
100 nm

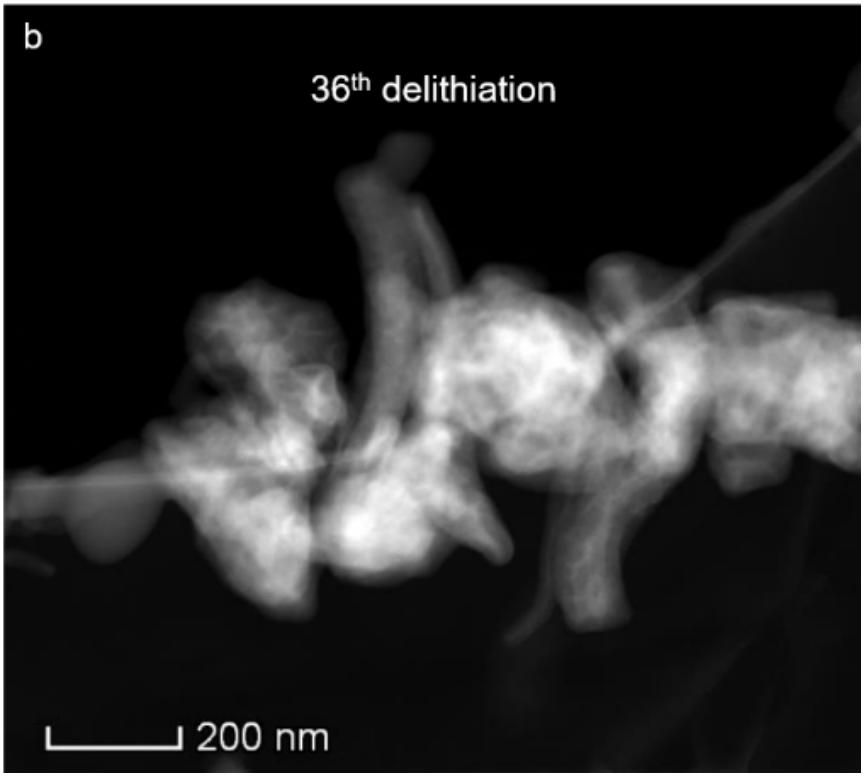
b
36th delithiation
200 nm

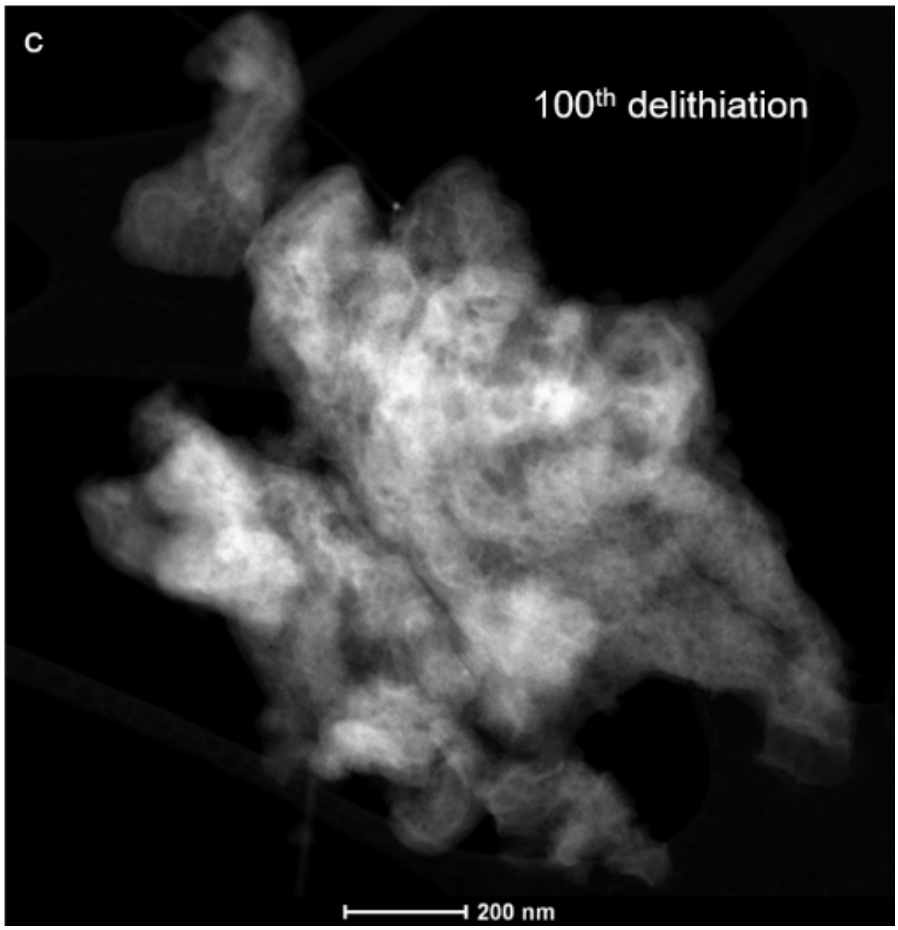

Supplementary Fig. 5 | Additional STEM-HAADF images of delithiated Si nanowires after different cycles to reveal the general feature of Si upon cycling. (a) 1st delithiated, (b) 36th delithiated, and (c) 100th delithiated. It should be pointed out that, the nanowires are not uniform in diameter and with long term cycling, the nanowire deform due to the growth of SEI towards the interior of Si. Also, for the Cryo-TEM sample preparation, we scratch off the sample. All these factors compounding together to make the sample loss the nanowire morphology, which is especially true for the sample following the extended cycling, as evidenced by comparing the case from 1 cycle, to 36 cycles and 100 cycles.

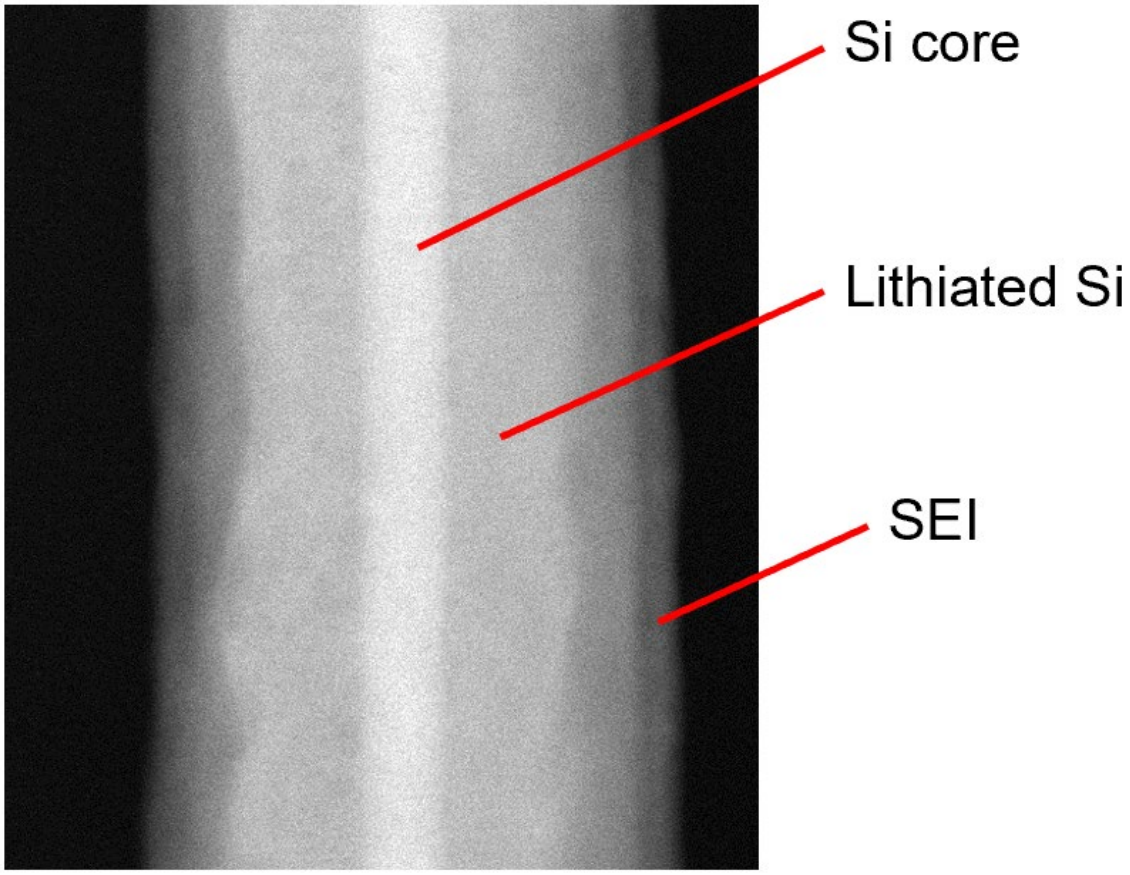

Supplementary Fig. 6 | STEM-HAADF image of a Si nanowire during the 1st lithiation showing the contrasts between pure solid Si core, lithiated Si and the SEI.

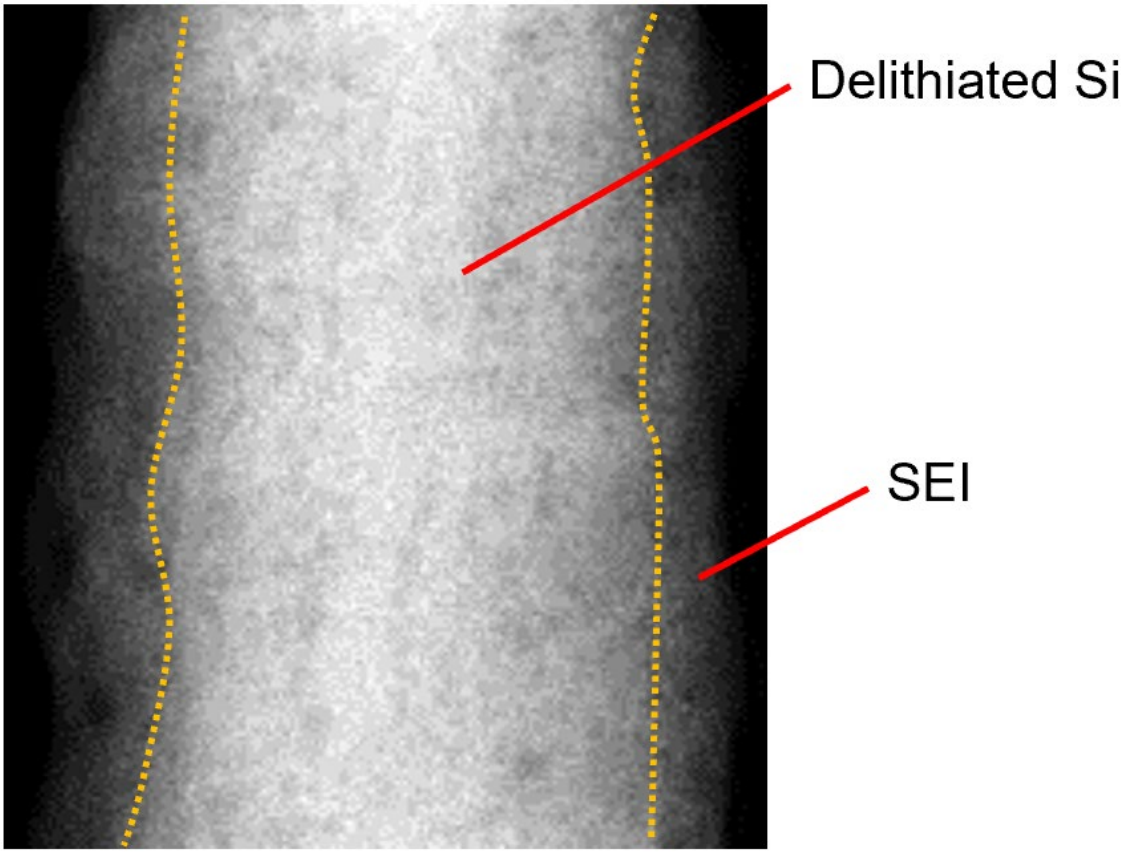

Supplementary Fig. 7 | STEM-HAADF image of a delithiated Si nanowire after 36th cycles.

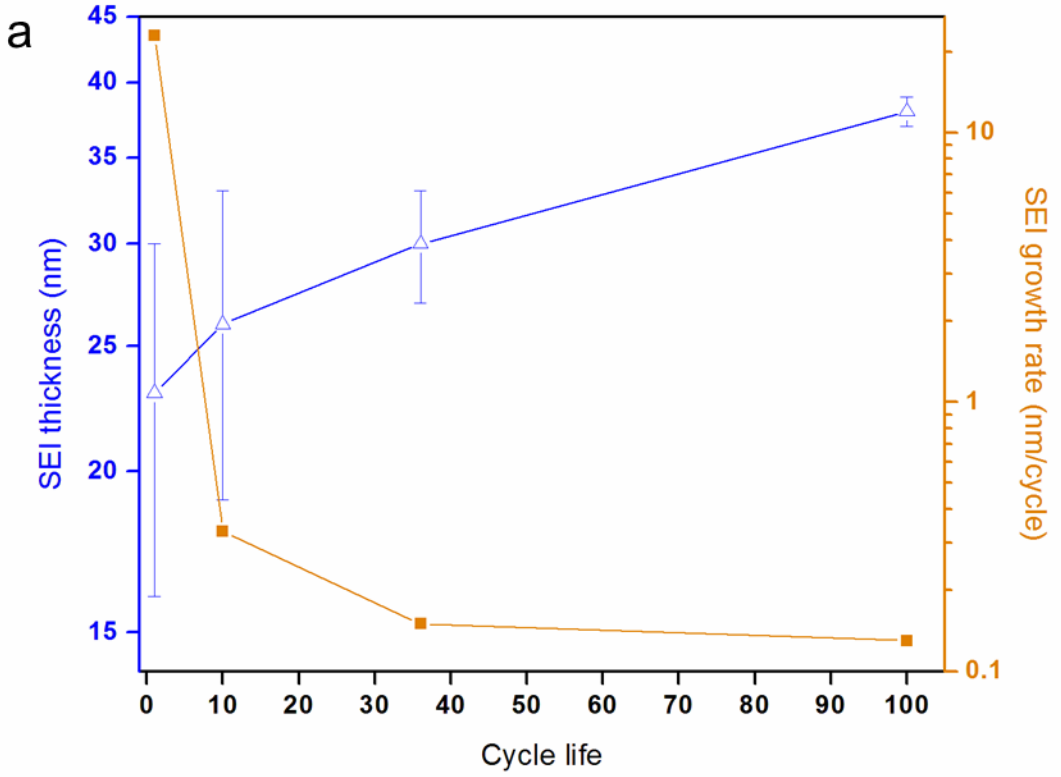
a
SEI thickness (nm)
SEI growth rate (nm/cycle)
Cycle life
45
40
35
30
25
20
15
10
1
0.1
0
10
20
30
40
50
60
70
80
90
100

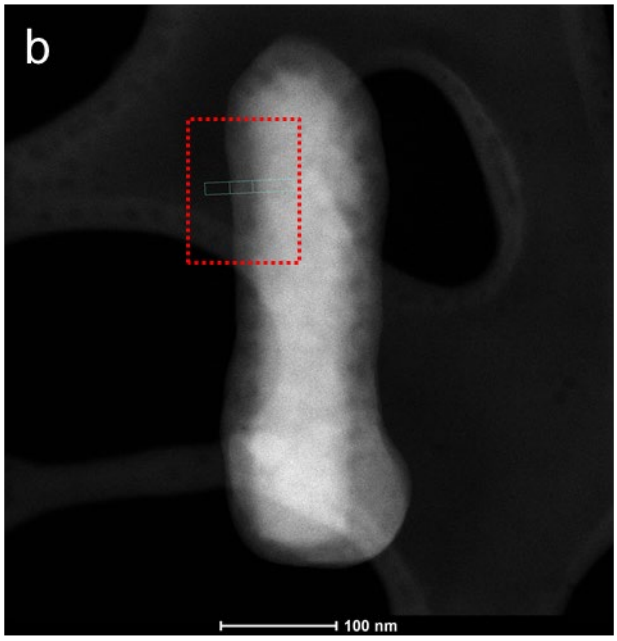
b
100 nm

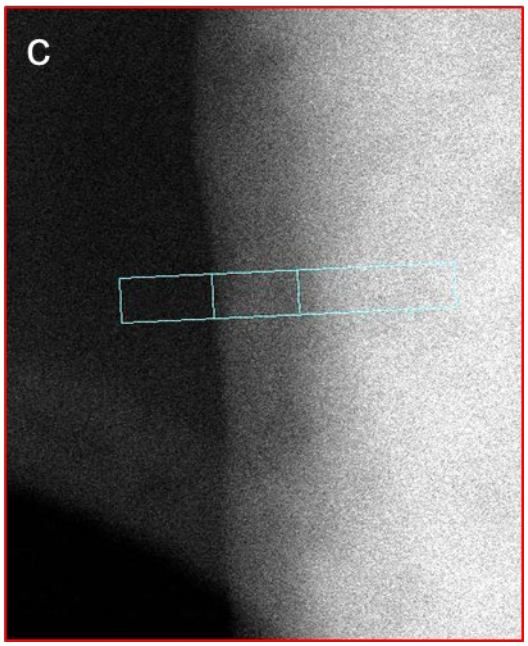
c

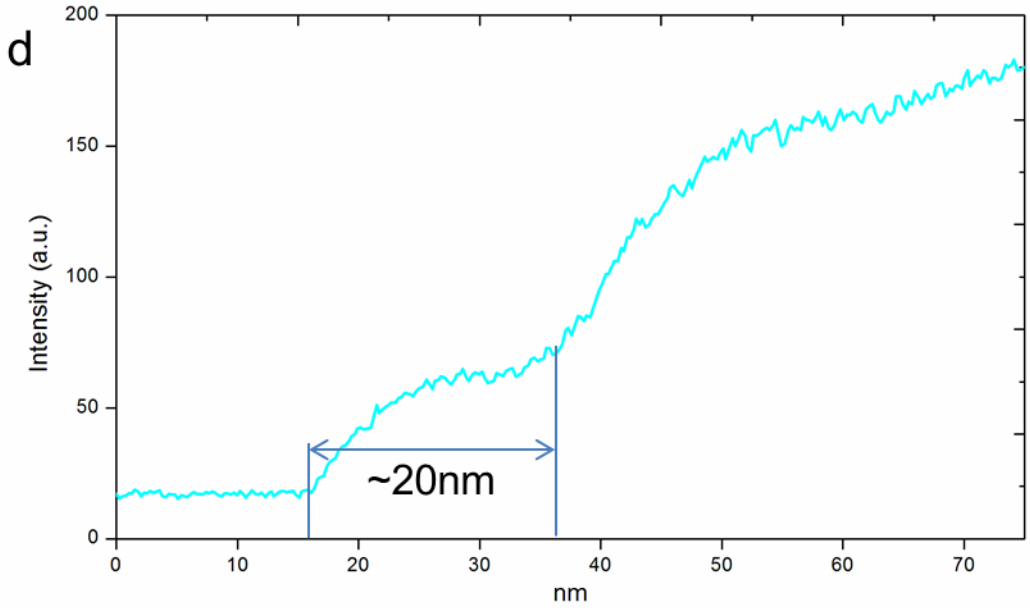

Supplementary Fig. 8 | SEI layer thickness and the growth rate upon cycling of the battery (a). The SEI thickness is directly measured from the STEM-HAADF images of the nanowires. Panel (**b-d**) shows the steps for the measurement. Regions with relatively clear contrast between the SEI and the delithiated Si core are chosen for the measurements, as shown in panel (**b-c**). By using the Digital Micrograph software, the corresponding STEM-HAADF intensity profile can be extracted as shown in panel (**d**). The thickness of the SEI is determined based on the intensity profile and the fact that SEI is relatively lighter than the delithiated Si core. Note that 5 independent measurements at different regions of 3 Si nanowires are used for each SEI thickness evaluation. The measurements here only provide an estimated value of the SEI, since the SEI thickness is not uniform on the Si nanowire surface and ice that is hardly avoidable in the cryo-TEM experiments may present on the Si nanowire (though ice is normally sputtered very quickly upon the zoom-in). The SEI growth rate is calculated by dividing the increment of SEI thickness using the cycle life increment.

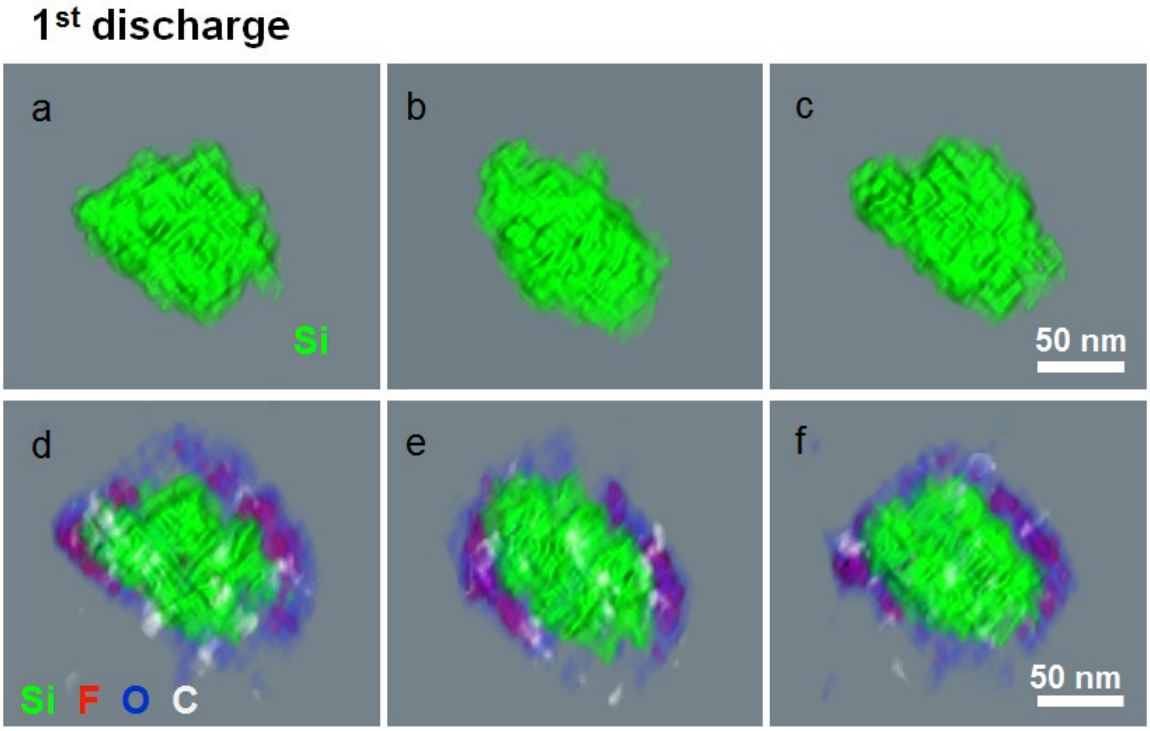

Supplementary Fig. 9 | Additional data showing segmented cross-section views for the 1st cycle nanowire without (a-c) and with (d-f) the SEI. The core is clearly integral. Contrast within the core can be attributed to the mass thickness difference due to the presence of pores within the core. The "core-shell" configuration of SEI/Si is clearly demonstrated. Slice thickness is 5 nm. Each element is color coded. It should be noted that C signal can be detected within the core which we believe is an artifact due to the carbon signals from the lacy carbon of the TEM grid.

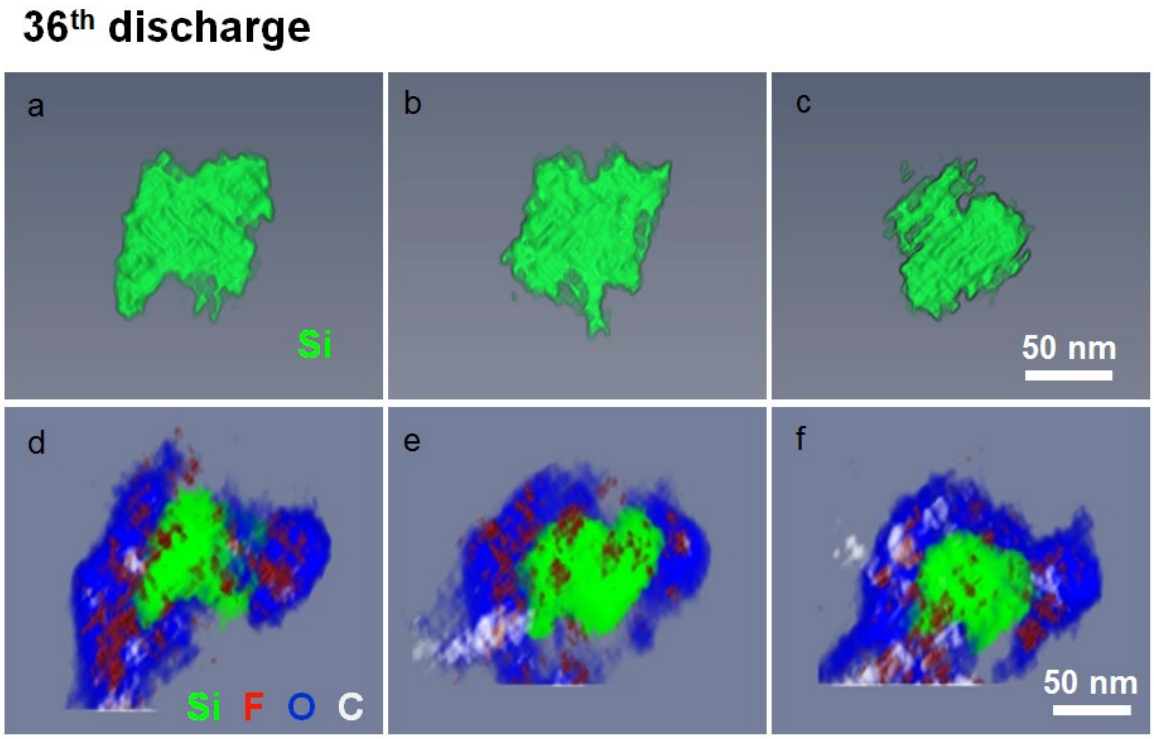

Supplementary Fig. 10 | Additional data showing segmented cross-section views for the 36th cycle nanowire without (a-c) and with (d-f) the SEI. The core is more damaged compared to that of the 1st cycle and remains relatively integral compared to that after 100 cycles (see following), which is consistent with the fact that the capacity retention at this stage is 94.5%. The SEI apparently starts to breach into the Si core, as non-trivial F is detected within the core region (also see Fig. 4b&e in the main text). Slice thickness is 5 nm. Each element is color coded.

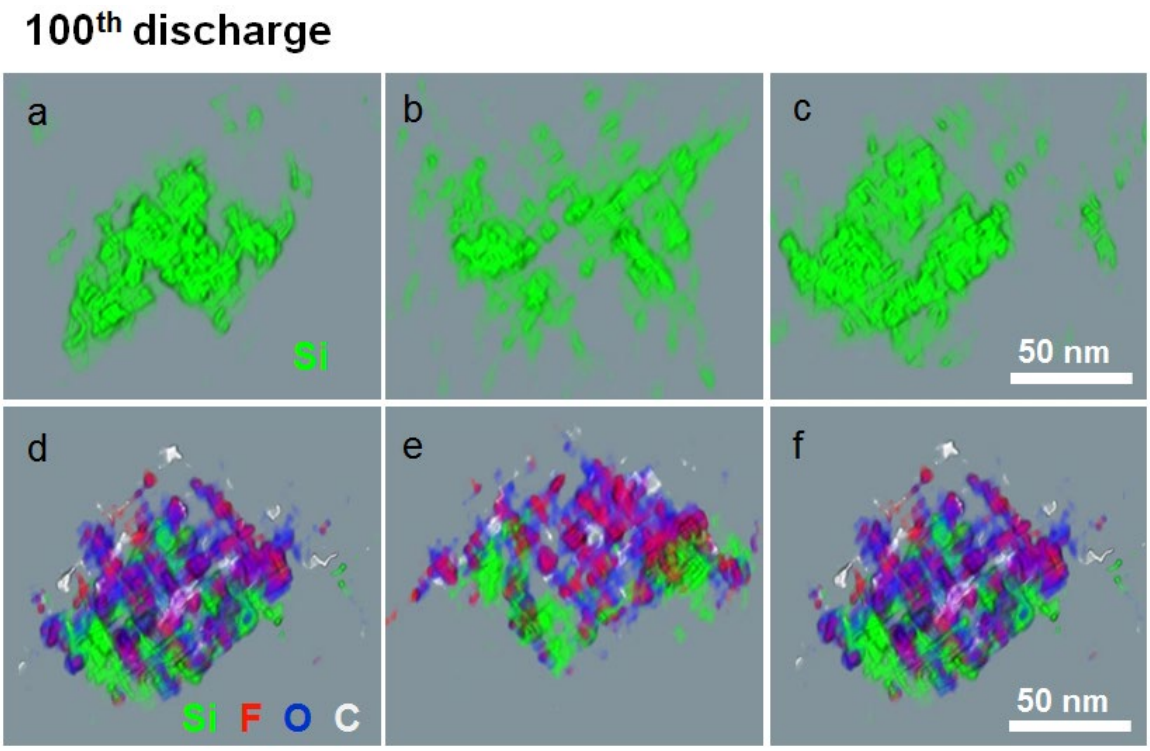

Supplementary Fig. 11 | Additional data showing segmented cross-section views for the 100th cycle nanowire without (a-c) and with (d-f) the SEI. The core is clearly disintegrated. The "core-shell" configuration of SEI/Si is clearly demonstrated. Slice thickness is 5 nm. Each element is color coded.

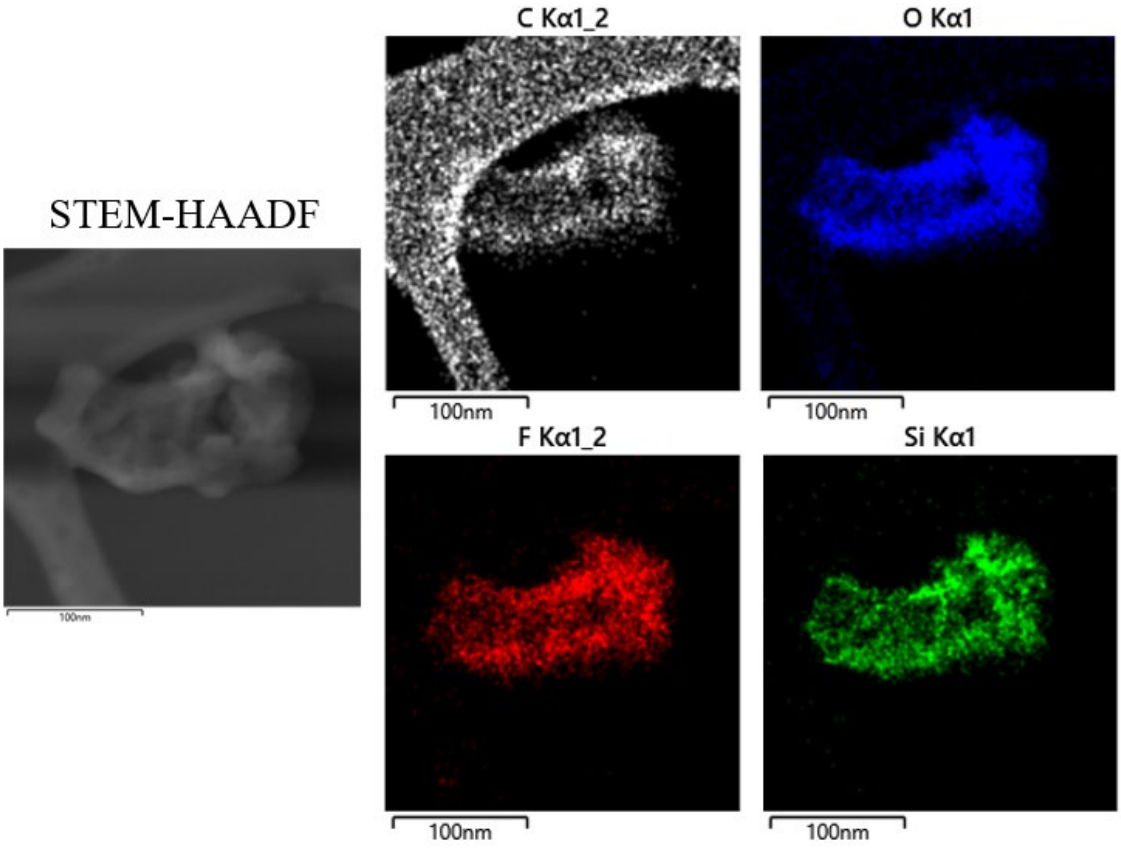

Supplementary Fig. 12 | Cryo-STEM EDS maps of the Si nanowire following 100 cycles at charged state, indicating similar structural feature as the case of discharged state.

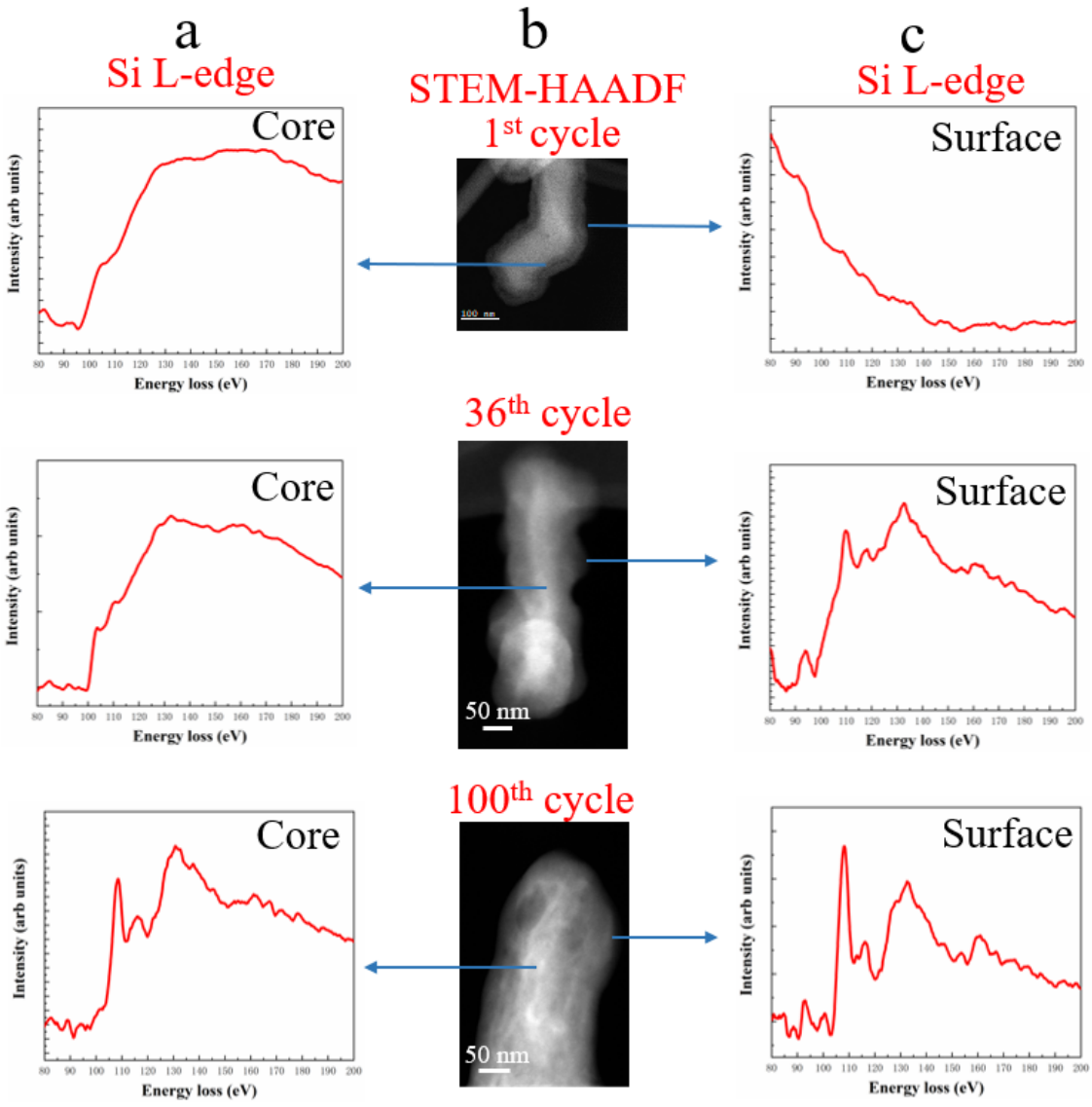

Supplementary Fig. 13 | Comparison of EELS of Si Li-edge of the Si nanowire following different cycles with that of Si and SiO_2. (a) Si L-edge from the core of the Si nanowire following1st, 36th, and 100th cycle. (b) STEM-HAADF image of the Si nanowire following1st, 36th, and 100th cycle. (c) Si L-edge from the surface of the Si nanowire following1st, 36th, and 100th cycle. The EELS indicates that following the 1st cycle, the surface shows no Si, indicating a SEI. With progressive cycling, the growth of SEI toward interior of Si lead to gradual oxidation of Si, especially at the surface.

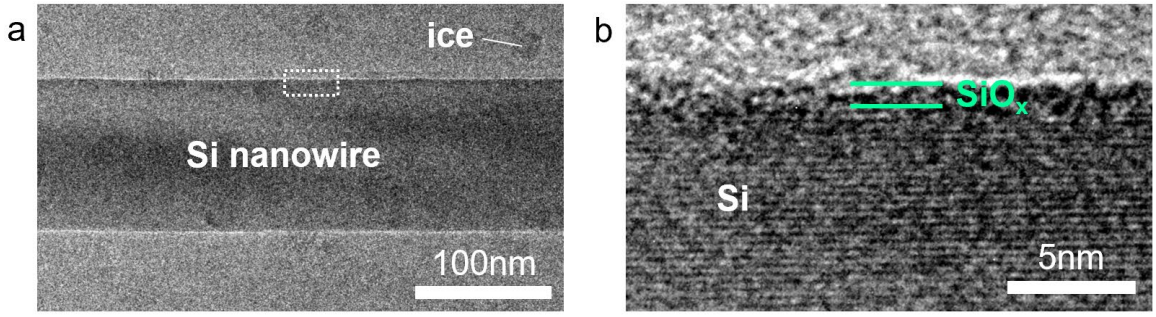

Supplementary Fig. 14 | Cryo-TEM characterization of the pristine Si nanowire. (a) Low magnification of the nanowire showing well-defined surfaces. The nanowire is supported on an amorphous carbon film on the TEM grid. Small ice pieces form due to the condensation of water vapor during the transfer of the cryogenic sample in air. (b) High magnification of the boxed area in panel (a), showing lattice fringes of the pristine crystalline Si nanowire and a thin layer of amorphous oxide on the surface.

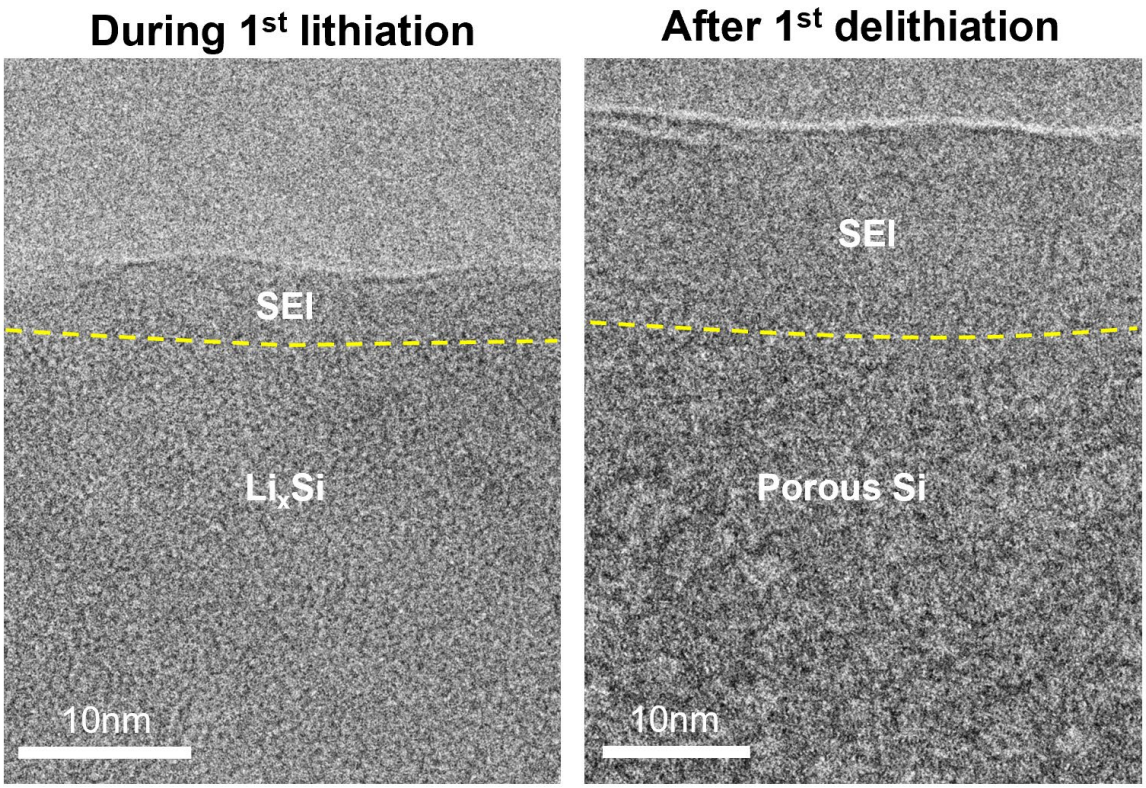

Supplementary Fig. 15 | Cryo-TEM image of the Si nanowire during and after 1st delithiation. Formation of pores ensuing the extraction of Li is clearly demonstrated. Dash line indicates roughly the position of the interface between SEI and the porous Si. Note that the SEI layer thickness measurement from such high resolution cryo-TEM images is not accurate due to the non-trivial electron beam sputtering effect.

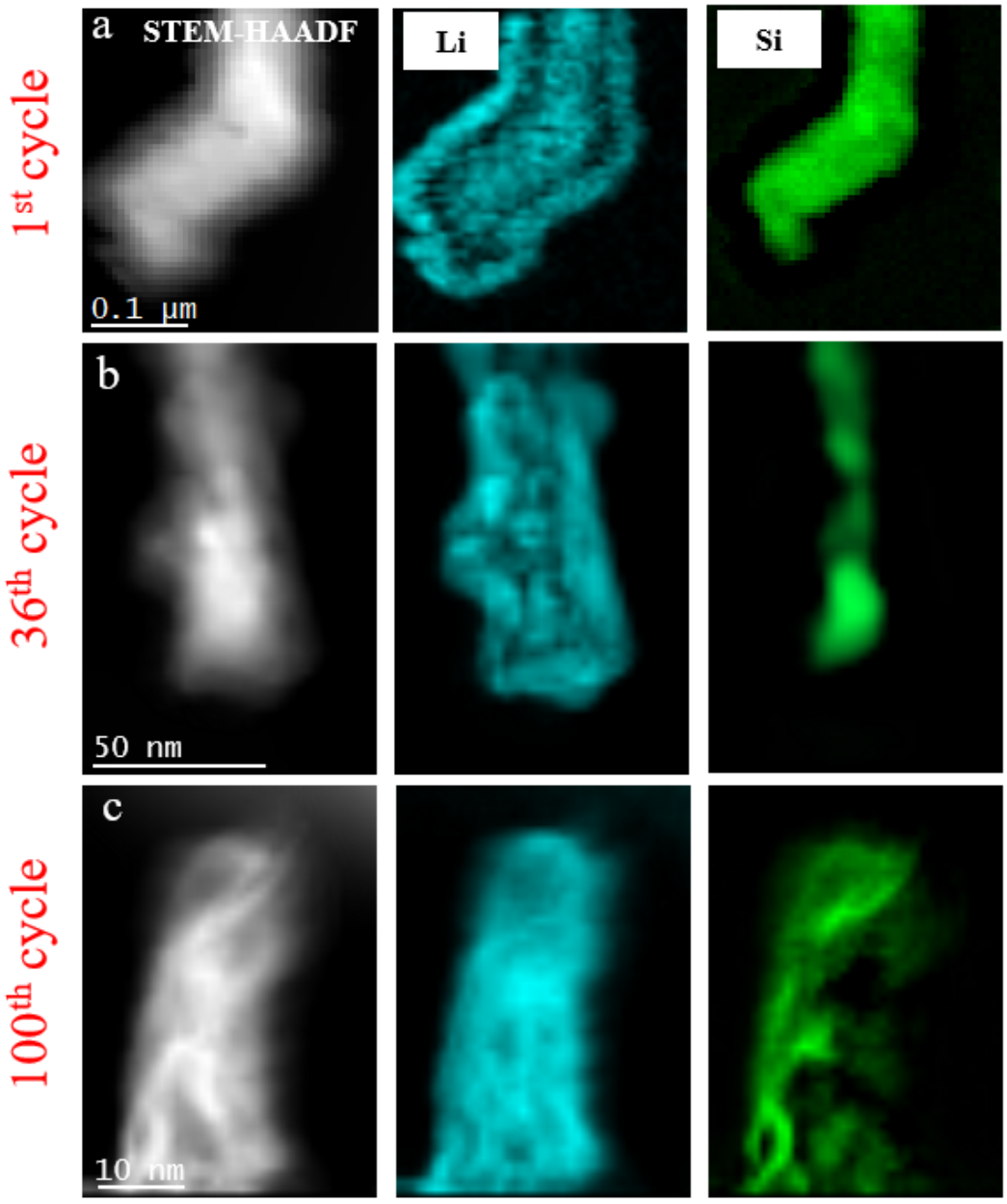

Supplementary Fig. 16 | STEM-HAADF image and Cryo-STEM EELS maps, showing the growth of SEI toward interior of Si leads to the "Li trapping" with gradual increased number of cycling.

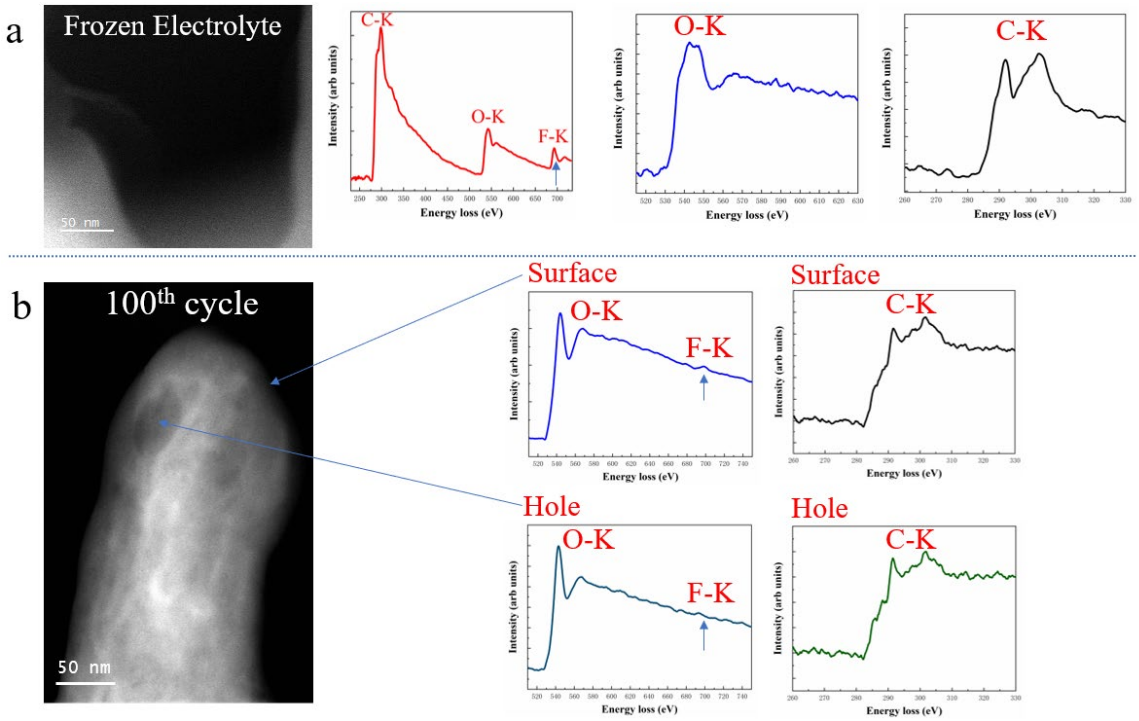

Supplementary Fig. 17 | STEM-HAADF image and cryo-STEM EELS to check if electrolyte is trapped in the void of Si following 100 cycles during the cryo-STEM sample preparation. (a) STEM-HAADF image and EELS of frozen electrolyte, featuring a strong F K-edge. (b) STEM-HAADF image and EELS of Si following 100 cycles, showing no strong F K-edge. Further, the EELS from the pore region is much similar with that from the surface region, consistently indicating SEI growth towards the interior of Si. All these demonstrate that the electrolyte does not trapped into the pore during the sample preparation.

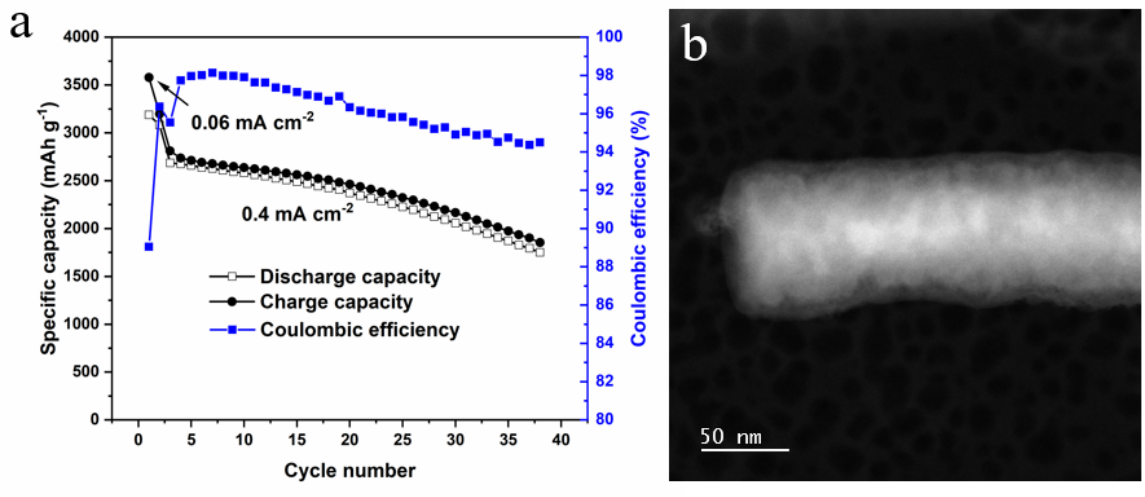

Supplementary Fig. 18 | Electrochemical properties and Cryo-STEM HAADF image of silicon nanowire cycled using electrolyte without FEC. (a) Capacity and Coulombic efficiency as a function of cycle numbers. (b) Cryo-STEM HAADF image showing the fluffy structure following 36 cycles at discharged state.

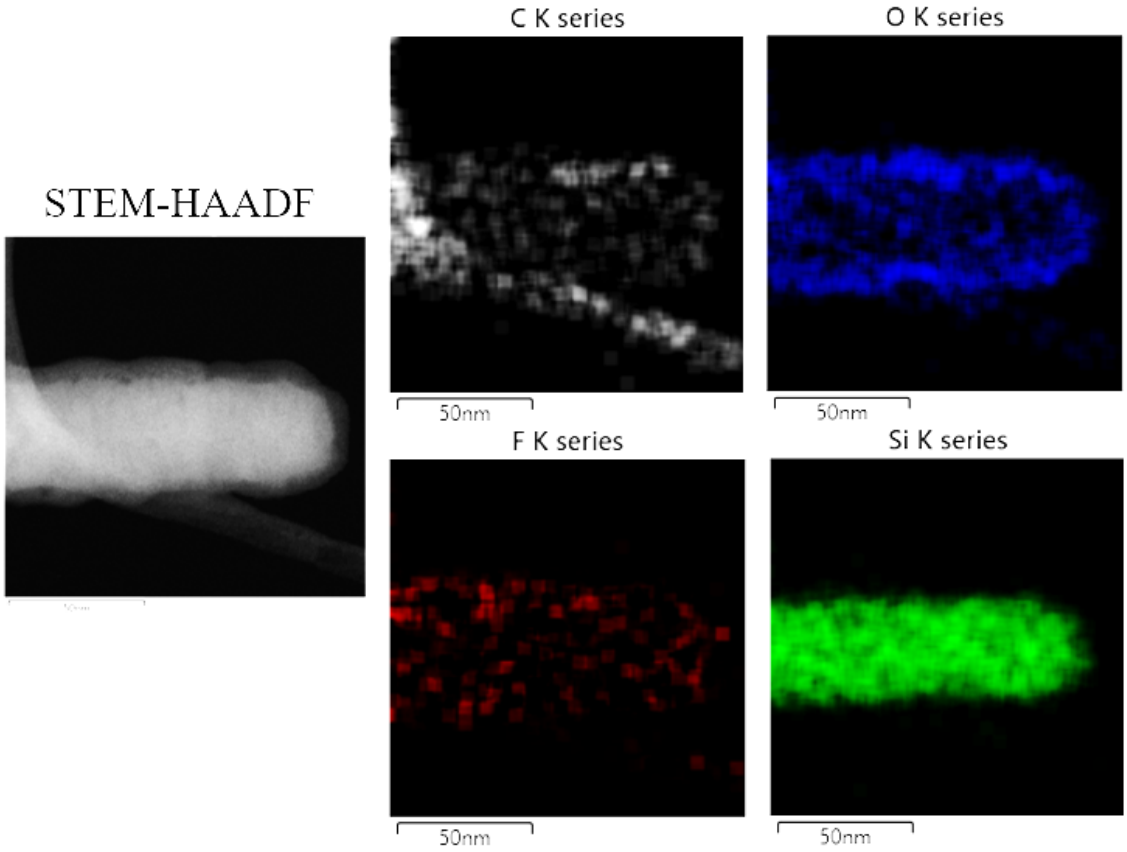

Supplementary Fig. 19 | Cryo-STEM EDS maps of the Si nanowire following 36 cycles at discharged state without FEC additive in the electrolyte, revealing SEI growth towards the interior of Si.

Evaluation of electron beam effect and optimization of imaging condition

To illustrate the beam damage is minimal, supplementary Fig. 20 illustrate the sample before and after the tomographic data acquisition.

The following effort has been made to minimalize the beam damage to the samples.

First, we studied how much irradiation samples can take under cryogenic conditions by varying the beam dose (controlled by beam current and acquiring time). As seen in supplementary Fig. 21, after acquisition with a beam dose of 8.9 $x10^6$ e/nm^2, some beam introduced voids start to form on the wire surface, but most part of SEI layer is still intact since the surface of the nanowire still look smooth. However, after exposure with beam dose over $1x10^7$ e/nm^2, the nanowire got toasted, the surface SEI layer was significantly sputtered, and more pores formed within the SEI and the nanowire. Based on the above facts, for all the tomography acquisition, we keep the total e-beam dose on the samples below $1x10^7$ e/nm^2 to avoid major beam damage. The total beam dose for the EDS tomography acquisition on Si nanowires after the 1st delithiation is 1.97 $x10^6$ e/nm^2. The total beam dose for the EDS tomography acquisition on Si nanowires after the 36th delithiation is 4.3 $x10^6$ e/nm^2. The total beam dose for the EDS tomography acquisition on Si nanowires after the 100th delithiation is 7.7 $x10^6$ e/nm^2.

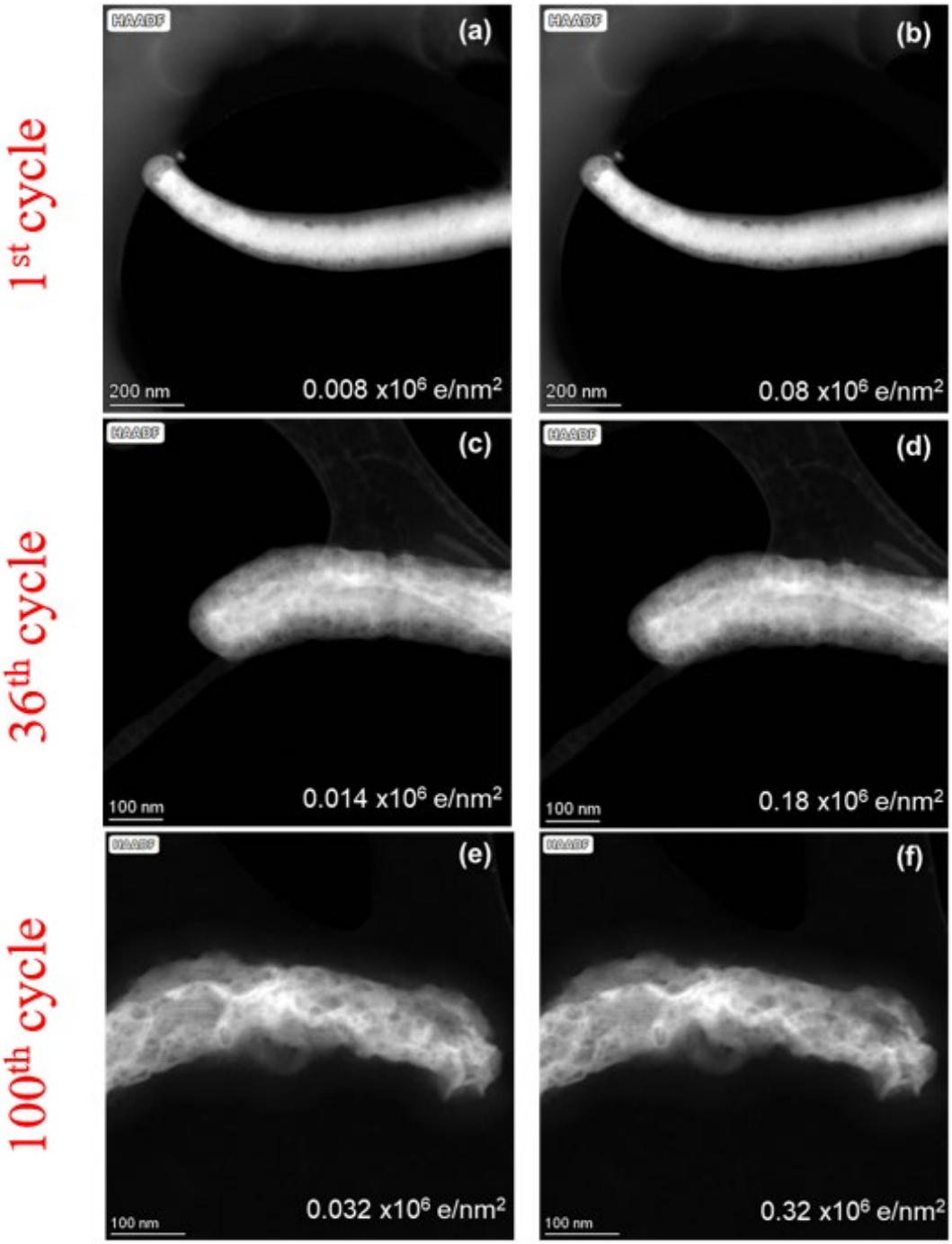

Supplementary Fig. 20 | Comparison of STEM-HAADF image of before and upon EDS tomographic mapping to assess the electron beam effect. a-b. The first (a) STEM image of a Si nanowire after the 1st delithiation and the STEM images of the same nanowire half-way through the EDS tomography (b). **c-d.** The first (c) and the last (d) STEM images acquired in the EDS tomography of a Si nanowire after the 36th delithiation. **e-f.** The first (e) and the last (f) STEM images acquired in the EDS tomography of a Si nanowire after the 100th delithiation.

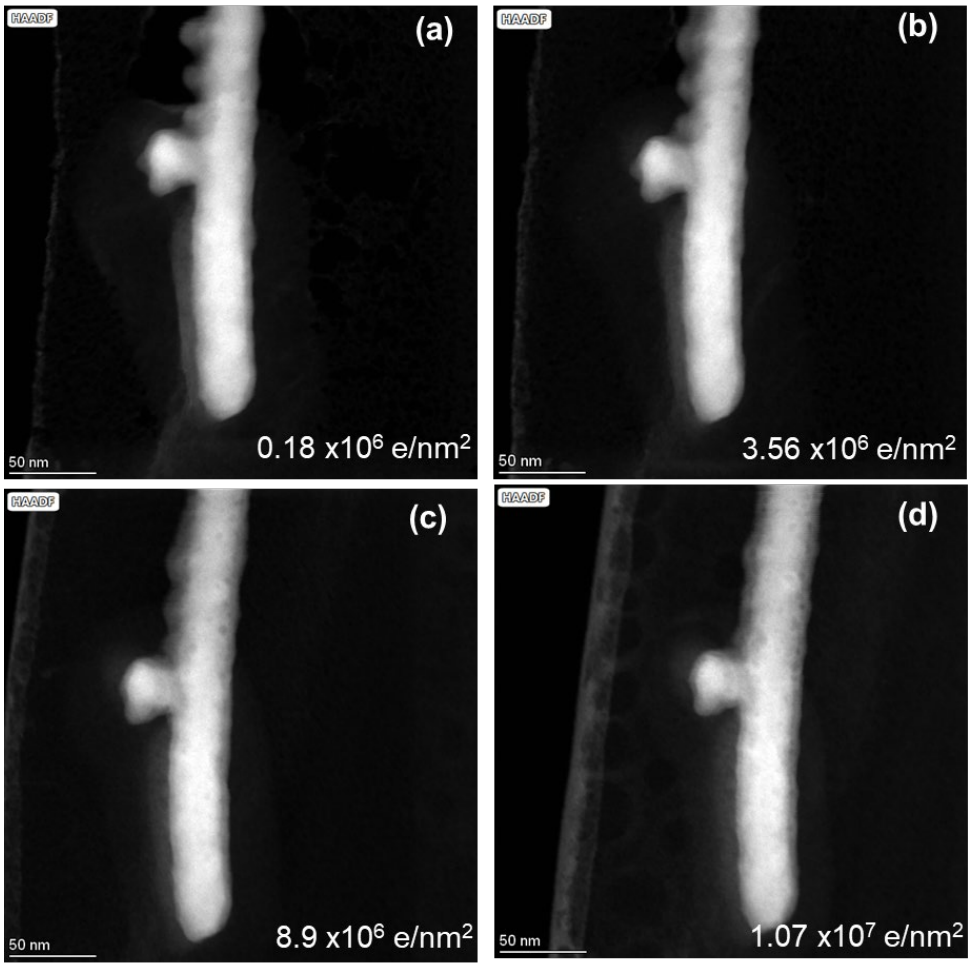

Supplementary Fig. 21 | STEM images of a Si nanowire after the 1st delithiation with different e-beam exposure dose with a probe current of 200 pA to evaluate the beam effect.

Additionally, we employed the following techniques to further minimize the beam damage to our samples during the EDS tomography acquisition.

1) the low-dose acquisition set-up has been utilized. As schematically shown in supplementary Fig. 22, to do tomography acquisition, we normally need to set up a tracking region to bias the drift of the sample and a focus region to set objective lens to desired defocus value at different tilts. Usually, these regions are set-up on the same region as the region of interest. For low-dose acquisition, we do automatic sample tracking and focusing not on the region of interest, but on nearby regions. In this way, we can minimize the beam exposure and thus the damage in the region of interest.

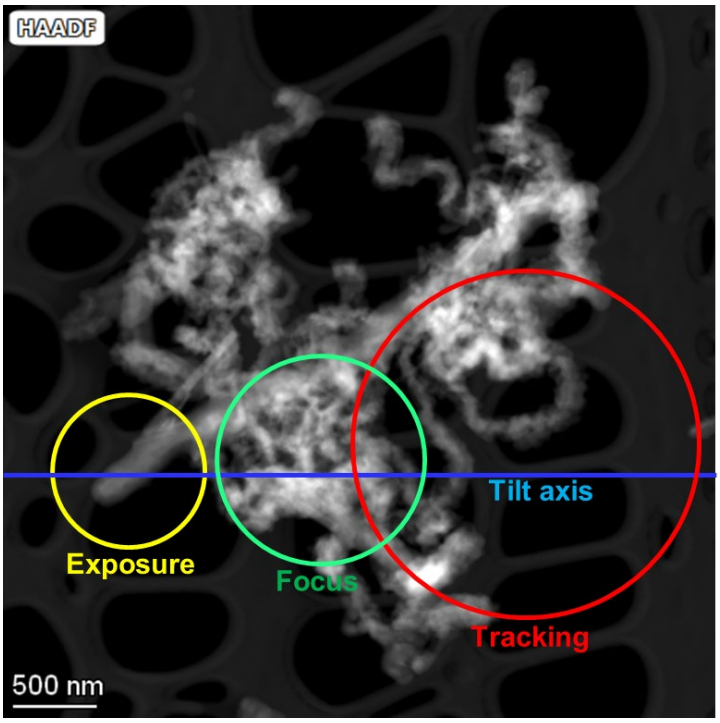

Supplementary Fig. 22 | Schematic to show the low-dose acquisition set-up. The red circle region is for tracking, the green region is for focusing, the yellow region is for the sample region of interest.

2) bidirectional tilt scheme had been employed in the acquisition. The different tilt schemes are shown in the supplementary Fig. 23 and more details can be found in the reference (Turoňová, B. *et al.* Benchmarking tomographic acquisition schemes for high-resolution structural biology. *Nat. Commun.* **11**, 876 (2020)). For bidirectional tilt scheme, the accumulated dose at low tilt angles is smaller compared to that of continuous tilt scheme, thus it provides the higher quality images for 3D reconstruction.

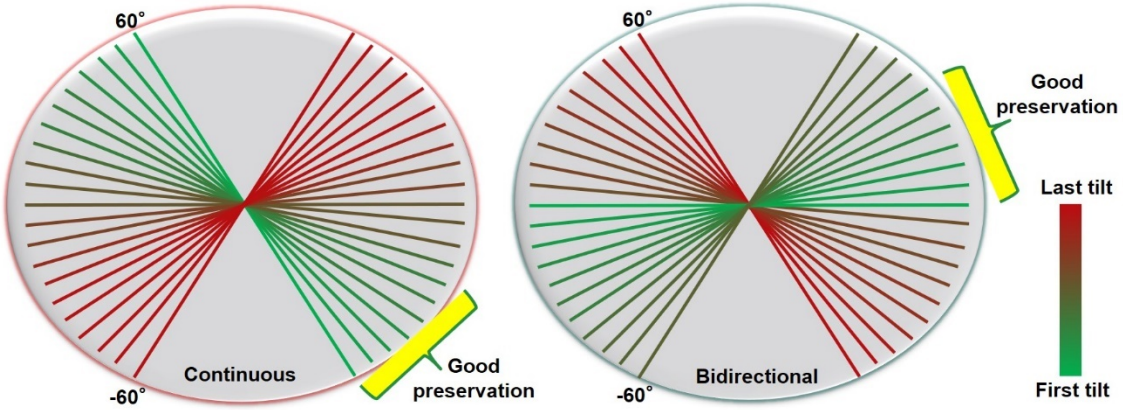

Supplementary Fig. 23 | Schematic to show the tilt scheme during the tomography acquisition.

By employing the advanced techniques as described above, beam-damage to the samples during the EDS tomography acquisition is significantly mitigated. As seen in supplementary Fig. 20, morphology of the Si nanowire looks very similar before and after the EDS tomography acquisition.

We studied beam dose effects on EDS signal and radiation damage, to determine the optimal dose and minimize radiation damage while maintaining required counts for reconstruction. Obviously, higher beam dose means more EDS signal for the reconstruction, but more radiation damage. The beam dose can be controlled by probe current and total acquiring time. We controlled the beam current at a range from 150 pA to 250 pA, since this is an empirical value for getting good EDS signal for beam-sensitive samples. We varied the total acquiring time and characterized the beam damage based on the HAADF morphologies with different beam dose exposure, as seen in supplementary Fig. 21. In this way, we can determine the total acquiring time of tilt series for avoiding a major beam damage. For example, after exposure to beam dose 8.9 x 10^6 e/nm^2, the sample start to get some damage, as seen in supplementary Fig. 21. We then kept the total acquiring beam dose for sample exposure to beam below this value. The total beam dose for the EDS tomography acquisition on Si nanowires after the 1st delithiation is 1.97 x10^6 e/nm^2. The total beam dose for the EDS tomography acquisition on Si nanowires after the 36 th delithiation is 4.3 x10^6 e/nm^2. The total beam dose for the EDS tomography acquisition on Si nanowires after the 100th delithiation is 7.7 x10^6 e/nm^2.

On the other hand, we studied how much acquisition time per tilt step we need to get enough signal for EDS quantification. As seen in supplementary Fig.24, after 100 s mapping time, the weight percentage of Si becomes stable with increasing mapping time.

Thus, to get reliable quantification result at each tilt, the minimum mapping time is at least 100 second.

Finally, the optimized time we found in our case is 114 s per tilt step, that is 45 mins in total acquiring time. With that mapping time, the Si counts approach 1000 at each tilt step as seen in supplementary Fig. 25, which is enough for EDS tomography reconstruction. The total dose of the Si nanowire undergoing throughout the tomography was 1.97 x 10^6 e/nm^2. With this optimal dose, we can avoid major beam damage and get enough counts for EDS quantification and reconstruction.

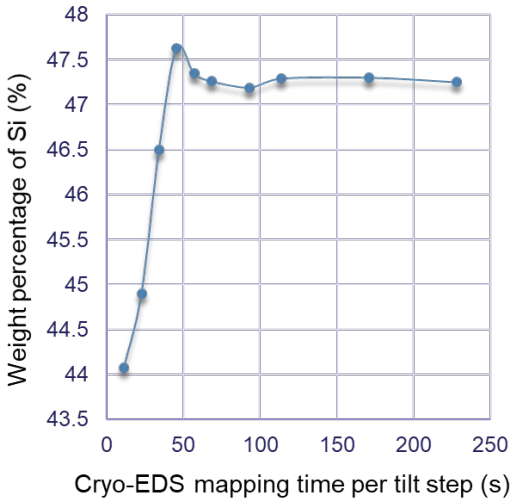

Supplementary Fig. 24 | Si element quantification result with increasing mapping time.

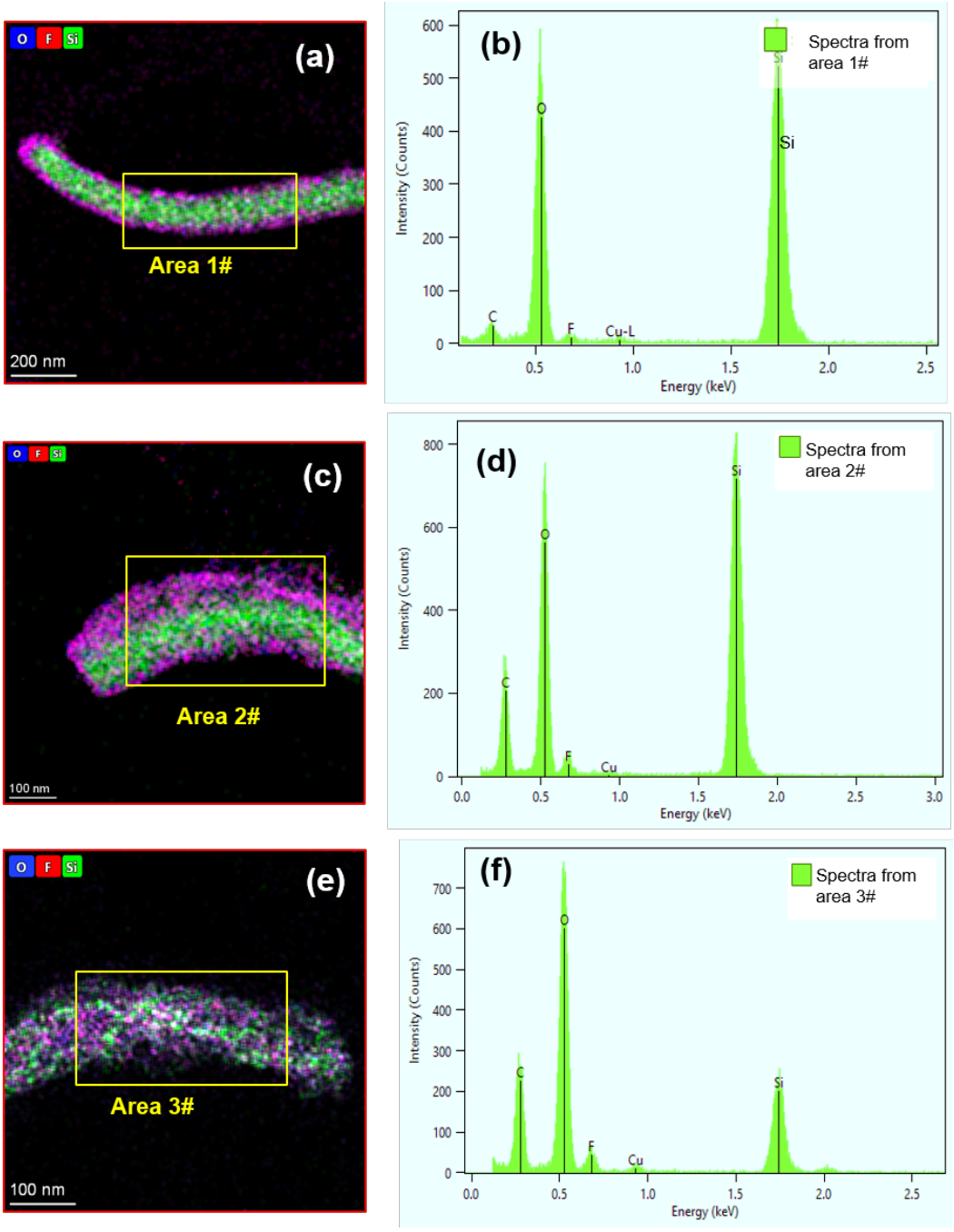

Supplementary Fig. 25 | EDS result of Si nanowires after different cycles. (a) elemental mapping and (b) corresponding spectrum of a Si nanowire after the 1st delithiation cycle; (c) elemental mapping and (d) corresponding spectrum of a Si nanowire after the 36th delithiation cycle; (e) elemental mapping and (f) corresponding spectrum of a Si nanowire after the 100th delithiation cycle. The background was subtracted using multi-polynomial model. The average filter (Kernel size 5 pixels) was applied for the maps to make elements more visible. (Note the peak at ~ 2 keV in (f) corresponds to P, which is a component of SEI layer).

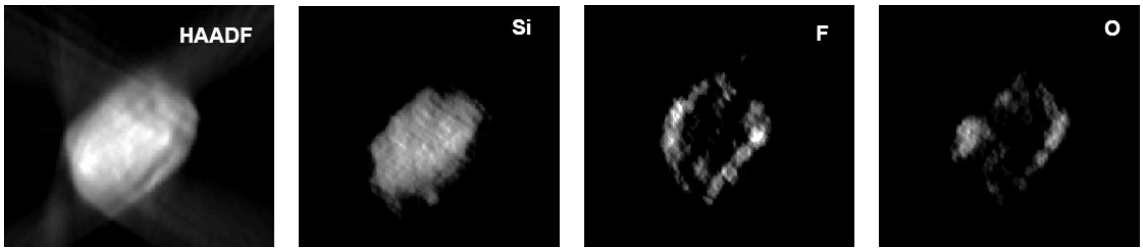

Supplementary Fig. 26 | Representative raw slices of cross sections of a Si nanowire after the 1st delithiation in the HAADF, Si, F and O reconstructions.

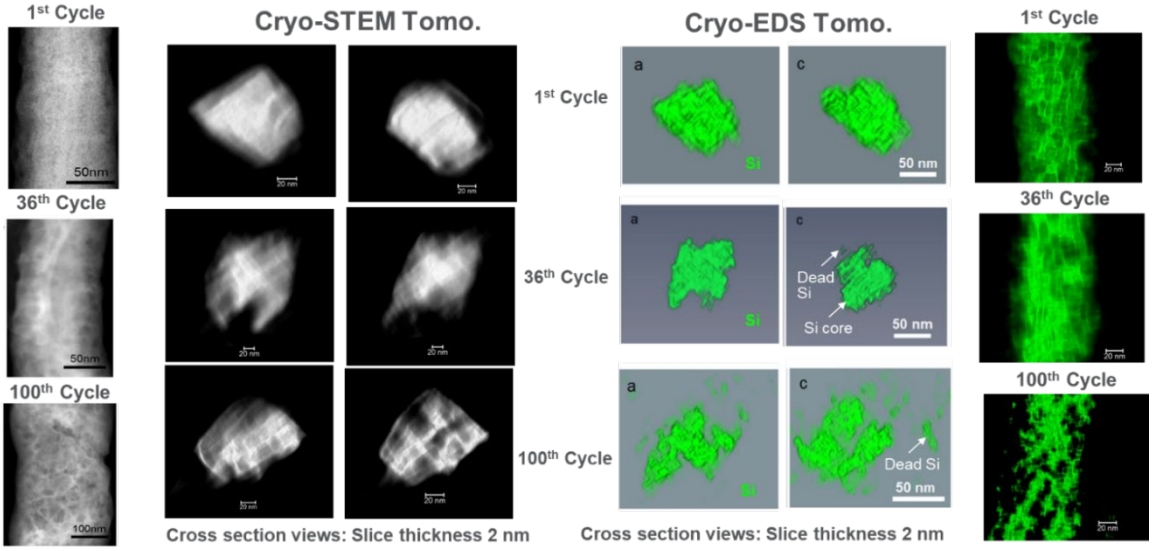

Supplementary Fig. 27 | Comparison of Cryo-STEM tomography with Cryo-EDS tomography results.

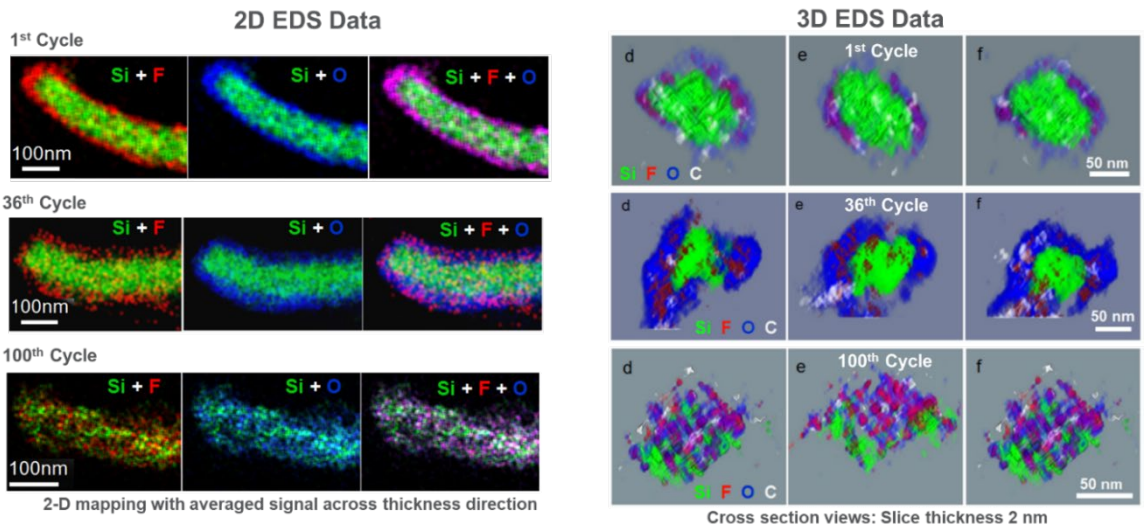

Supplementary Fig. 28 | Comparison of 2D EDS maps with 3D EDS tomography results.

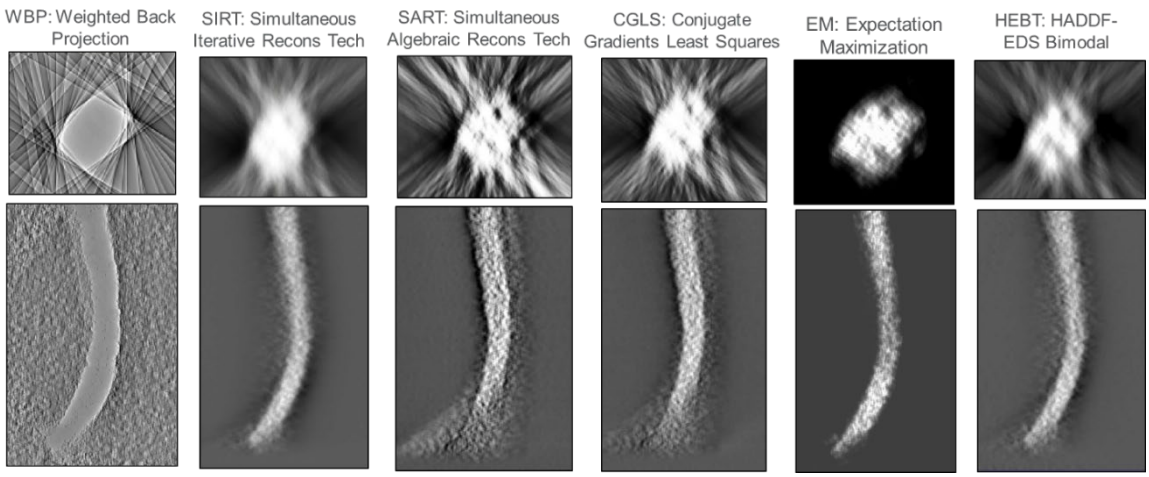

Supplementary Fig. 29 | Compassion of Si (Net EDS counts) reconstruction slices using different algorithms in Inspect 3D. The advantage of using Expectation-Maximization is that it reduces the elongation of particles and dampens more missing wedge artifacts. In statistics, the Expectation-Maximization algorithm is an iterative method to find (local) maximum likelihood or maximum a posteriori (MAP) estimates of parameters in statistical models, where the model depends on unobserved latent variables (Sigworth, F. J., Doerschuk, P. C., Carazo, J.-M. & Scheres, S. H. W. An introduction to maximum-likelihood methods in cryo-EM. *Methods Enzymol.* **482**, 263-294 (2010)). Expectation-Maximization is more or less like simultaneous iterative reconstruction technique (SIRT) and it is actually also known as multiplicative SIRT (as opposed to the additive SIRT).

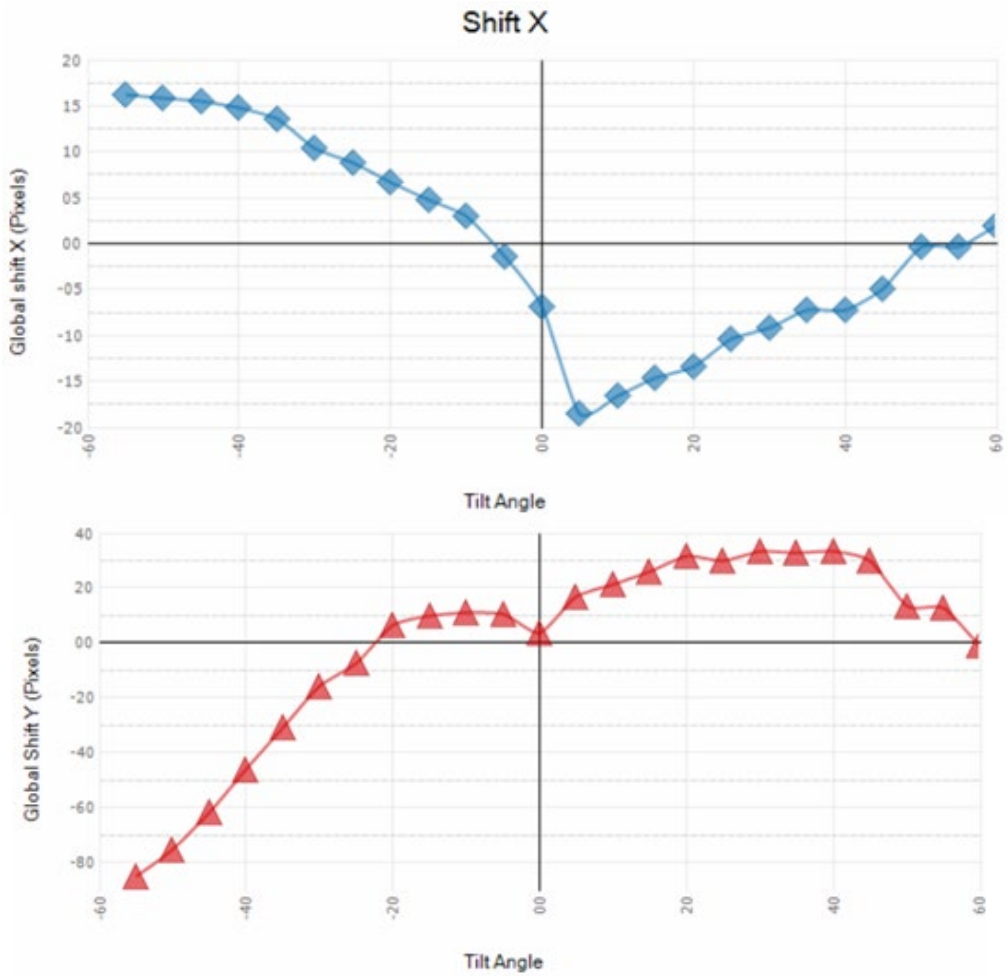

Supplementary Fig. 30 | A typical shift X and shift Y data after the stack alignment for tilt series. Each pixel is equal to 2.13 nm.

Additional information about the background and signal intensity

For spectrum processing, a multi-polynomial model was used for the background correction. The energy peak used for Si fitting is 1.7397 keV; for O fitting is 524.9 eV; for F fitting is 676.8 eV; for C fitting is 277.4 eV. As a representative case, the Supplementary Fig. 31 shows the raw spectrum overlayed with the spectrum after the background subjection (the dark outline).

The spectrum shown in the Supplementary Figure 25 is fitted to derive the peak to background (P/B) ratio, which is conveniently defined as ratio of the net counts at the energy window of a specific element divided by the background counts at the same energy window of that specific element. The net count for Si is located at the energy window from 1.662 keV to 1.818 keV; for O 461eV to 587 eV; for F 626 eV to 726 eV; and for C 231 eV to 321 eV. For the sample of 1^{st} cycle: the calculated P/B ratio is 2.9 for F; 75 for O; 62.4 for Si; and 11.6 for C. For the sample of 36^{th} cycles: the calculated P/B is 4.6 for F; 51.5 for O; 51.3 for Si; and 37.7 for C. For the sample of 100^{th} cycles: The calculated P/B ratio is 25.2 for F; 288 for O; 73.5 for Si; and 195 for C.

All the EDS maps inputted for the reconstruction were background subtracted.

One of the fundamental concerns for the EDS tomography is the weak signal, consequently limiting the attainable resolution. Therefore, it is important that the peak of the element in concern can be identified. To illustrate this, the as-acquired spectrum counts per pixel are provided in supplementary **Figs. 32**, **33** and **34**. As shown in the colored mappings and the extracted spectrums at typical 1x1 pixel regions in the supplementary **Figs. 32**, **33**, and **34**, we can clearly locate the elements in concern.

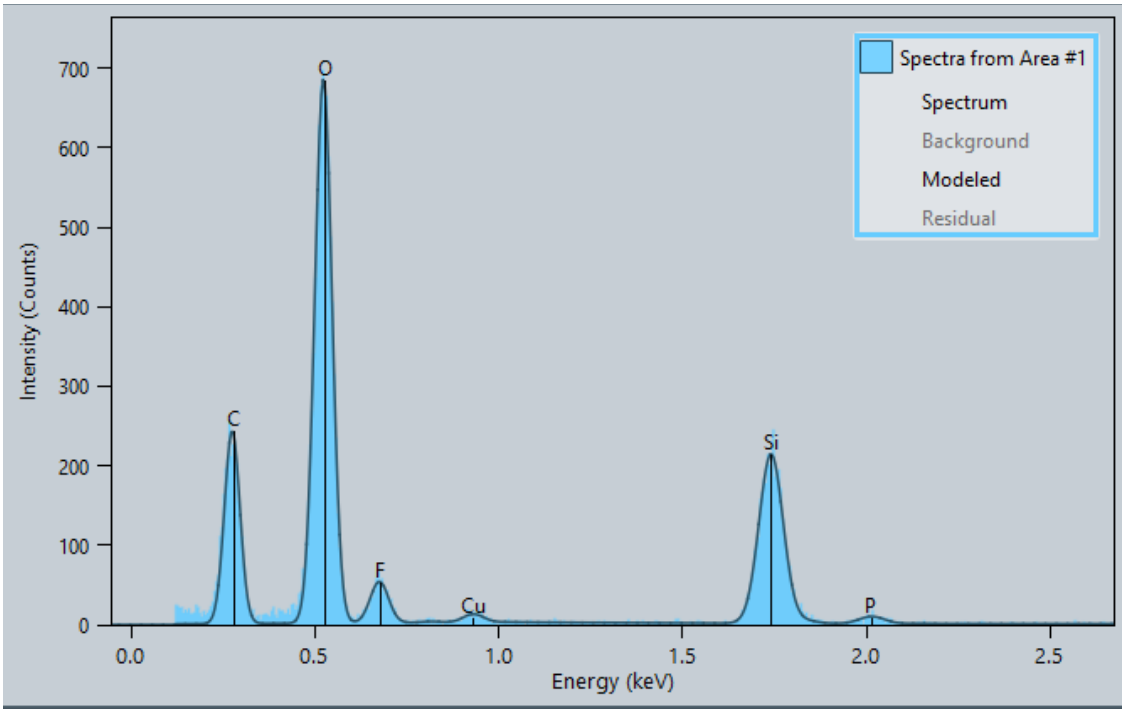

Supplementary Fig. 31. Spectrum background subtraction. The spectrum from the sample of 100th cycles. The blue area is the raw spectrum. The multi-polynomial model was used for the background correction, leading to the background corrected spectrum shown by the dark line. The energy peak used for Si fitting is 1.7397 keV; for O fitting is 524.9 eV; for F fitting is 676.8 eV; for C fitting is 277.4 eV.

To further vividly demonstrate the data quality, we show the spectrum collected from the nanowire and that collected from the supporting carbon film (pixel point #5 in supplementary **Figs. 32, 33, and 34**), demonstrating that the EDS signals of the element in concern at each single pixel region on the nanowire can be seen. It is apparent that elements O, F related to SEI are indeed present in the interior of the Si nanowire after the 100th cycle; and as for nanowires after the 1st cycle, these elements of SEI only present on the surface of the Si nanowire. In other words, the key finding of our work, that is the "SEI inward growth towards the interior of Si", is well substantiated by our Cryo-EDS-Tomography.

To illustrate how much signal is spread in the maps, especially for the case of F as representative case, we show the intensity distribution at each pixel in the supplementary **Fig**. **35** and **Fig. 36** for the case of 1st cycle and 36 cycles respectively. Apparently, at each pixel the count for F is above the background.

Further, we show the spectrum in the feature of 5x5 pixels as Supplementary **Fig. 37**, where all the elements can be clearly identified, even including the peak of P at the energy position of ~ 2 keV, which is a component of SEI and is apparently visible following the 100th cycles.

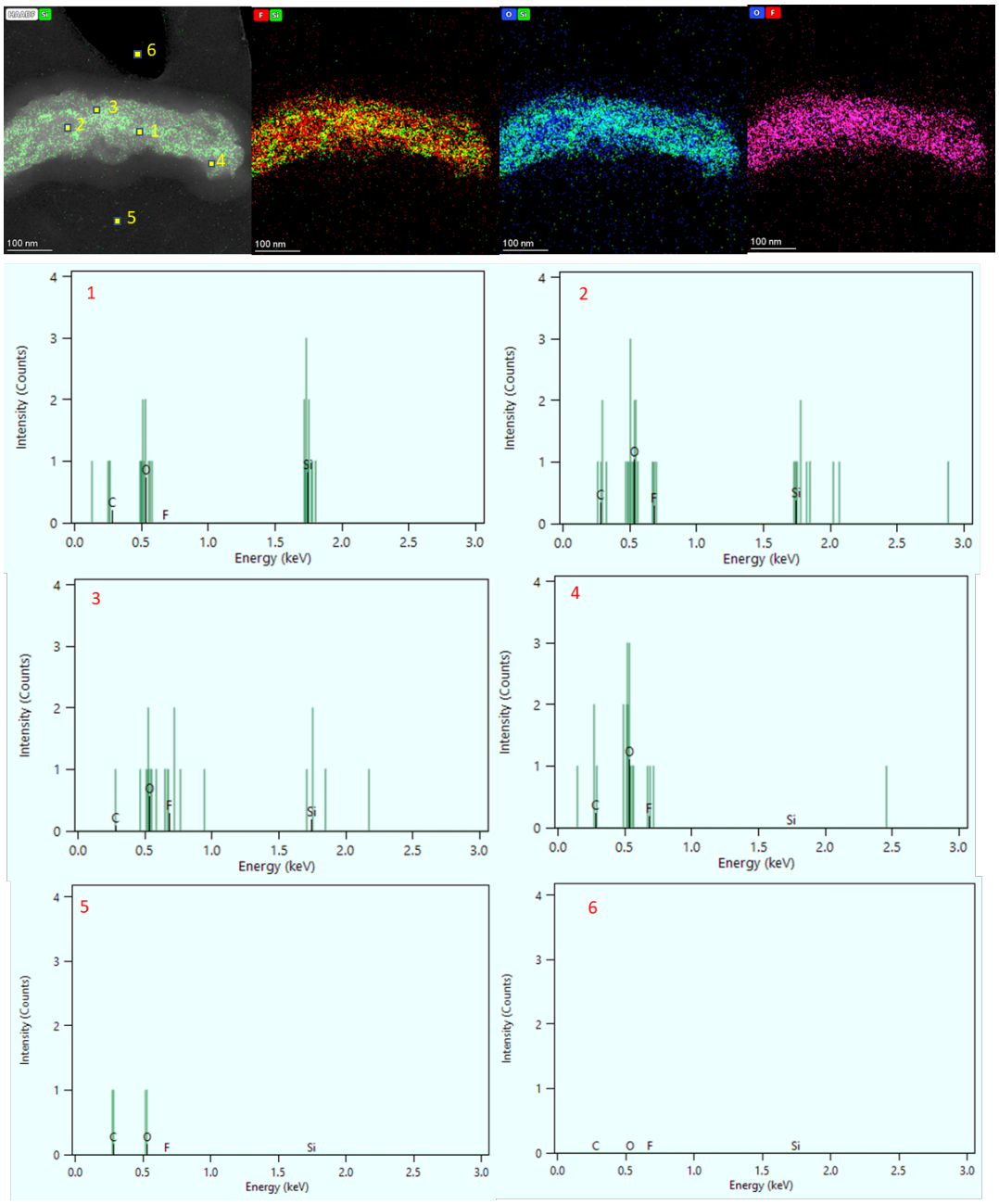

Supplementary Fig. 32 | The spectrum extracted from 1x1 pixel region (pixel size 1.068 nm) at different locations for the sample following 100th cycle. All the spectra were extracted from 2D mapping at each tilt angle, and they were not from reconstruction tomography. By comparison of the spectrum at different pixels, we can tell the distribution of elements. It should be noted that in the spectrum2, the counts at ~ 2 keV corresponds to P, which exists in the SEI layer following 100th cycles.

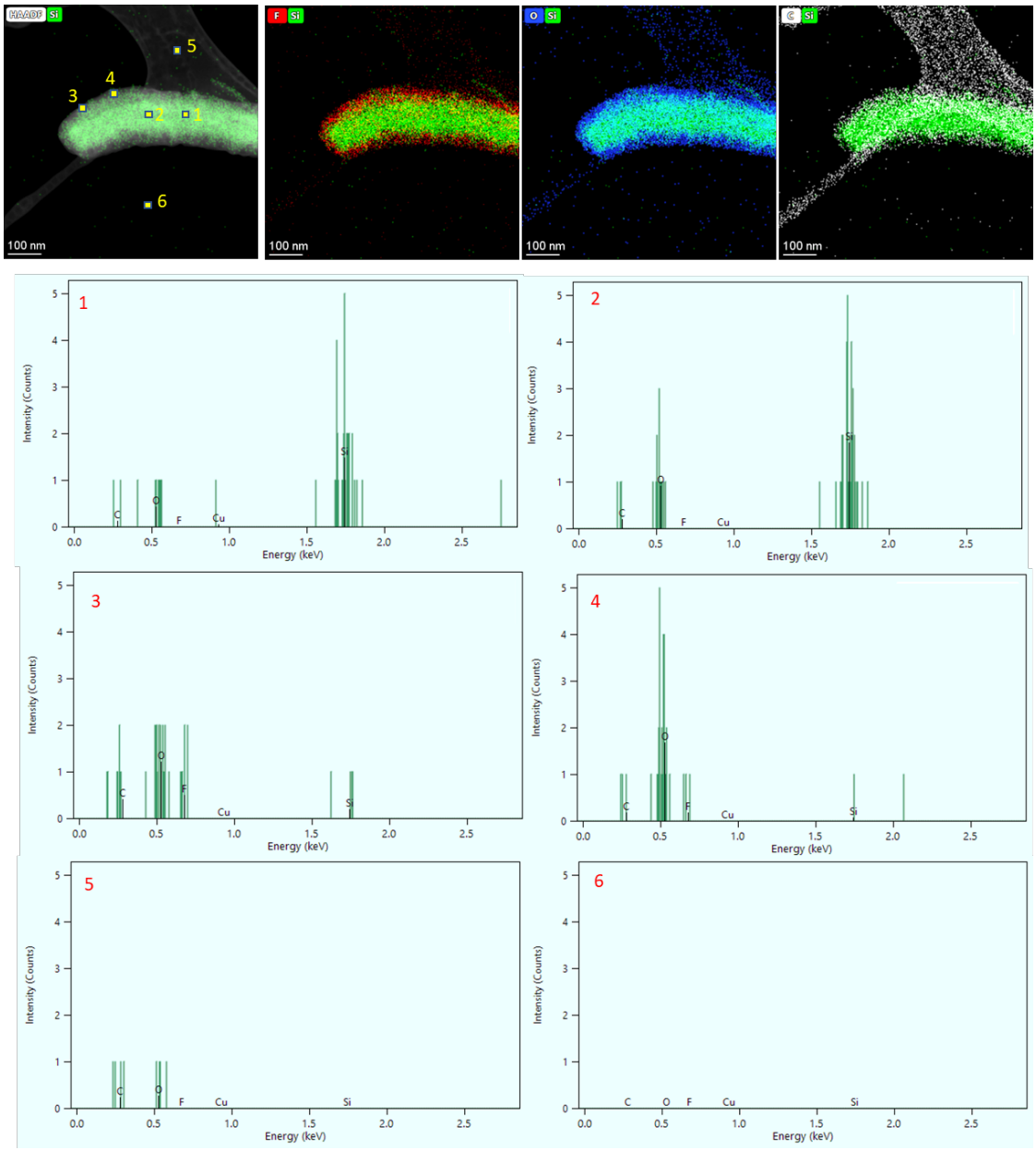

Supplementary Fig. 33 | The spectrum extracted from 1x1 pixel regions (pixel size 1.48 nm) at different locations for the sample following 36th cycle. All the spectra were extracted from 2D mapping at each tilt angle, and they were not from reconstruction tomography. By comparison of the spectrum at different pixels, we can tell the distribution of elements.

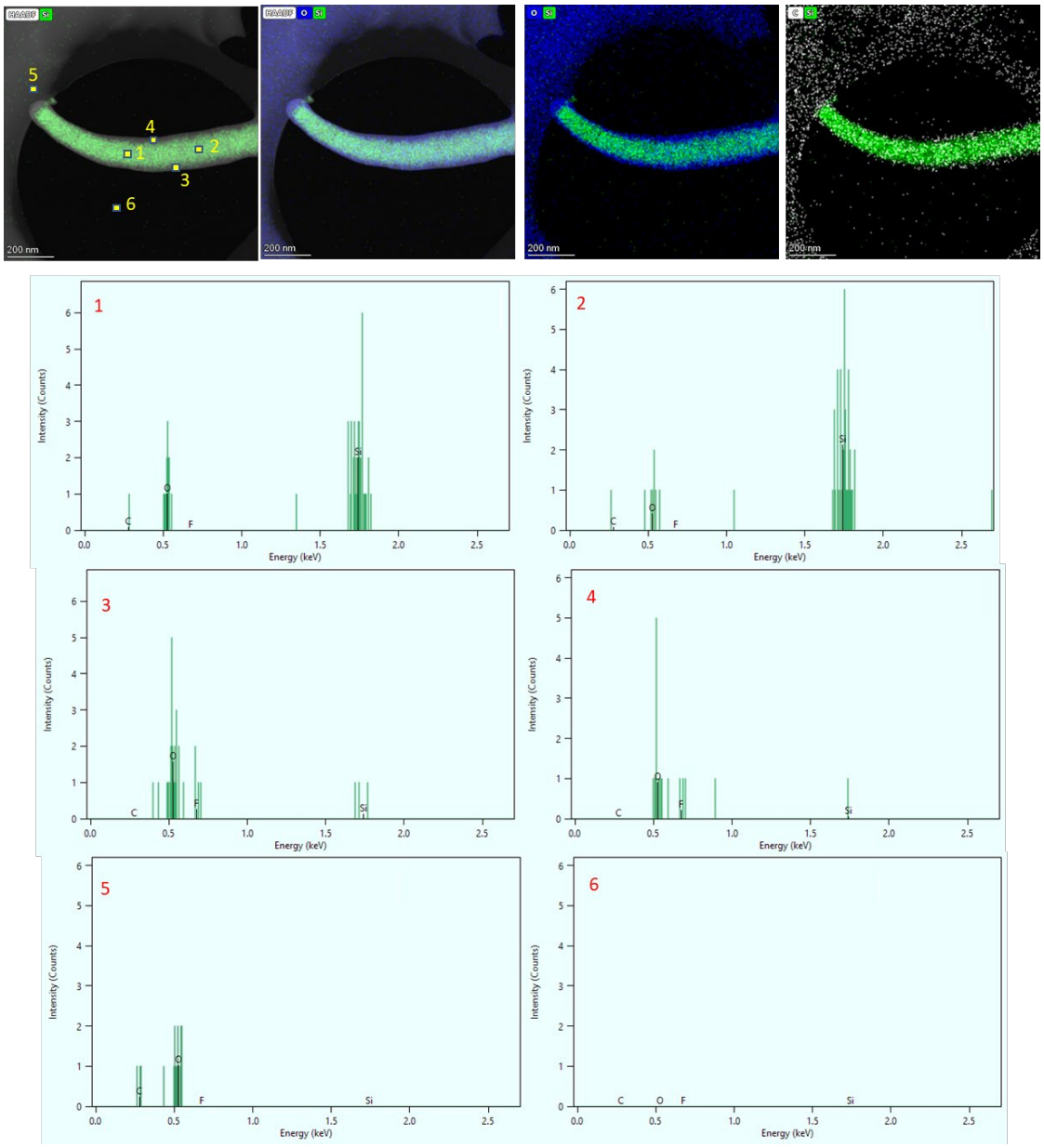

Supplementary Fig. 34 | The spectrum extracted from 1x1 pixel regions (pixel size 2.134 nm) for the sample following 1st cycle. All the spectra were extracted from 2D mapping at each tilt angle, and they were not from reconstruction tomography. By comparison of the spectrums at different pixels, we can tell the distribution of elements.

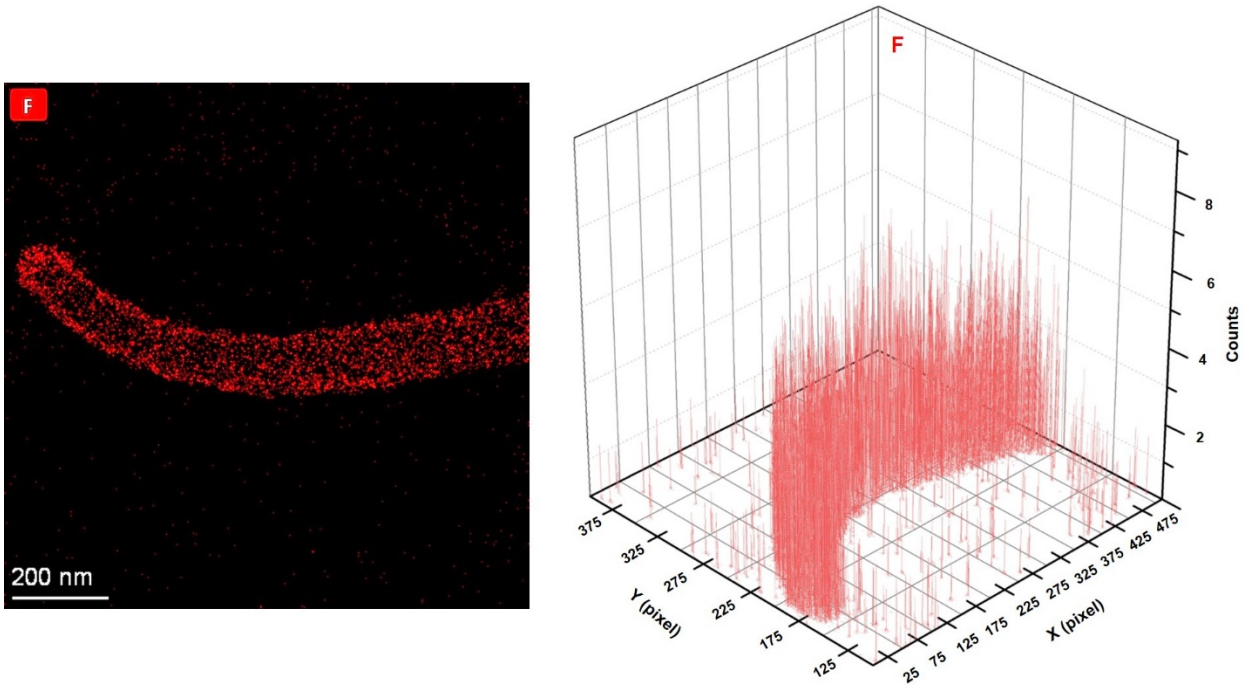

Supplementary Fig. 35 | F Count distribution at 1x1 pixel for the sample following 1st cycle. The left panel is the 2D map of F distribution. The right panel is the F count distribution at each pixel as captured spectrum, illustrating the counts distribution at each pixel for F.

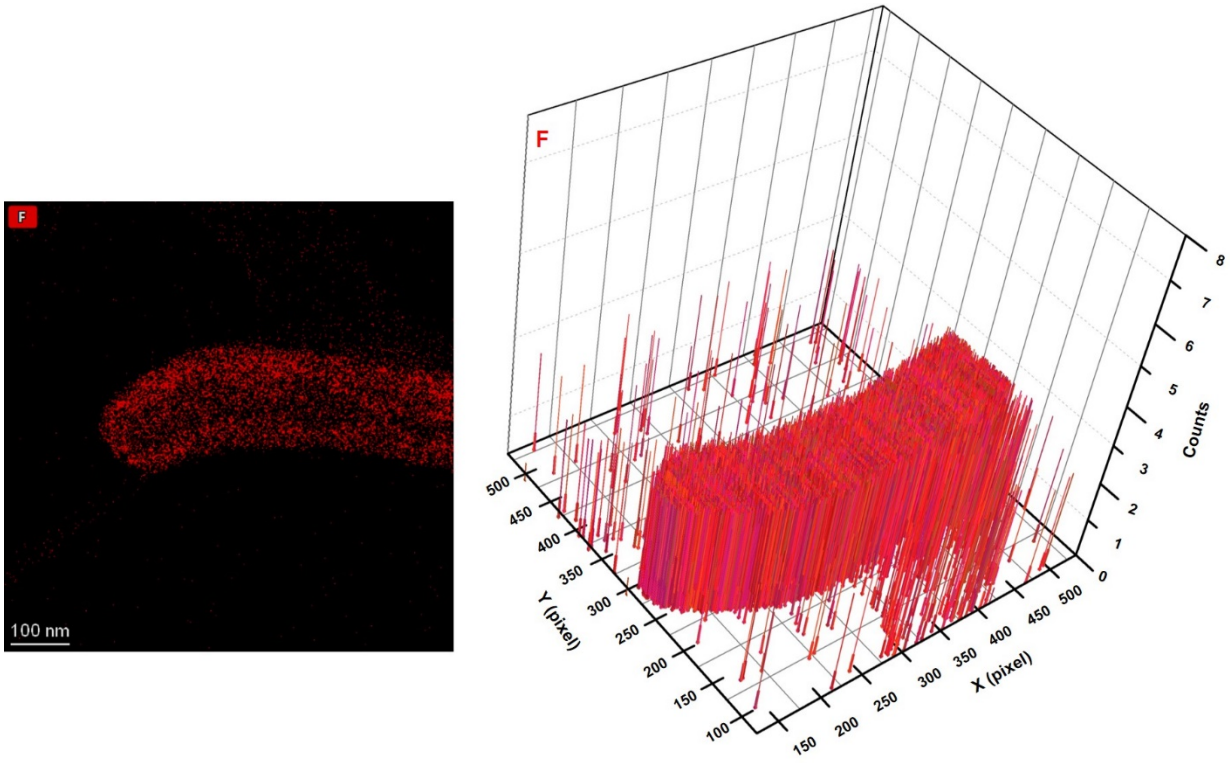

Supplementary Fig. 36 | F Count distribution at 1x1 pixel for the sample following 36th cycle. The left panel is the 2D map of F distribution, right is the F count distribution at each pixel as captured spectrum, illustrating the counts distribution at each pixel for F.

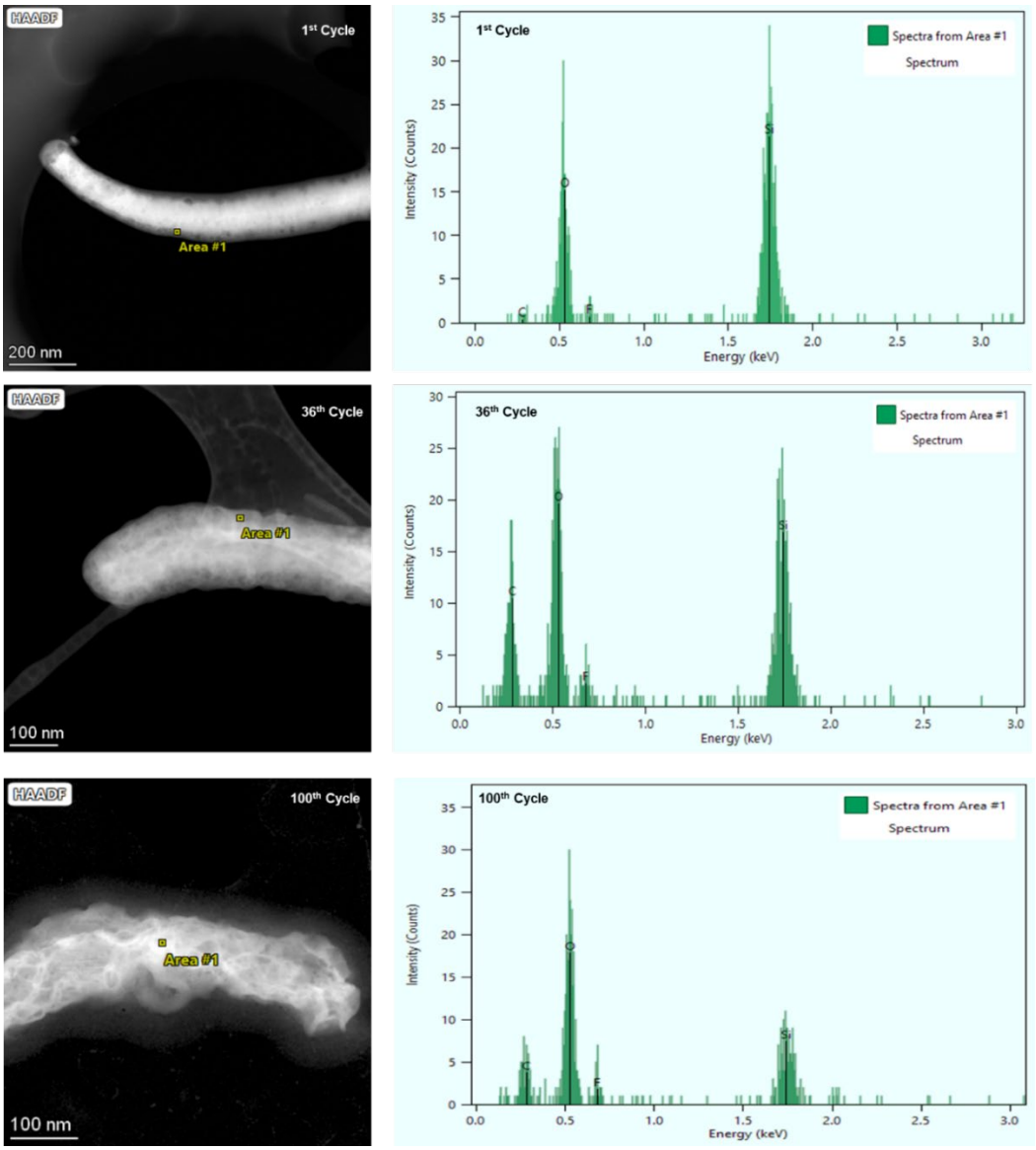

Supplementary Fig. 37 | The spectrums from typical small feature regions (5x5 pixels) to show the counts with each element. The top panel is the 1st cycle; The middle panel is the 36th cycle; and the bottom panel is the 100th cycle. Note the peak at ~ 2 keV corresponds to P, which is a component of SEI layer and is detected following the 100th cycling.

Supplementary Discussion

Surface morphology evolution does not correlate to the corrosion of Si

Firstly, pure hydrofluoric acid can only etch the SiO_x oxide on the nanowire surface but hardly with Si. In our sample, a uniform 1~2 nm SiO_x layer presents on the Si nanowire surface, which cannot account for the observed severe surface morphology changes. Additionally, should certain corrosion reaction happen, Si would be expected to present in the SEI or electrolyte. However, barely any Si is found in the SEI or electrolyte after cycling, as evidenced by the elemental mapping data of the SEI (Fig. 2b) and the inductively coupled plasma mass spectrometry data on the residual electrolyte from a similar cell[1]. Moreover, despite the obvious surface morphology changes, the capacity loss after 36 cycles is very low (~5.6%, see Method for the calculation), indicating that the surface morphology changes are not due to materials loss.

Supplementary Table 1. Parameters used in the simulation of morphological evolution

Parameter	Symbol	Normalization	Value
Energy barrier coefficient	Ω	$\Omega/(c_{\max}\mathrm{RT})$	2.6
Gradient energy coefficient of c_{Li}	κ_{Li}	$\kappa_{\mathrm{Li}}/(c_{\max}\mathrm{RT}l_0^2)$	0.0001
Gradient energy coefficient of c_{v}	κ_{v}	$\kappa_{\mathrm{v}}/(c_{\max}\mathrm{RT}l_0^2)$	0.00001
Volumetric change coefficient	β		0.5874
Elastic modulus of pure/unlithiated silicon	$E_{\max}$	$E_{\max}/(c_{\max}\mathrm{RT})$	175
Elastic modulus of lithiated silicon	$E_{\min}$	$E_{\max}/(c_{\max}\mathrm{RT})$	43.75
Yield strength	σ_{Y}	$\sigma_{\mathrm{Y}}/(c_{\max}\mathrm{RT})$	1.64
Mobility of lithium	M_{Li}	$\mathrm{M}_{\mathrm{Li}}(c_{\max}\mathrm{RT}\Delta t)/l_0^2$	10
Mobility of vacancy	M_{v}	$\mathrm{M}_{\mathrm{v}}(c_{\max}\mathrm{RT}\Delta t)/l_0^2$	0.1
Maximum concentration	$c_{\max}$		0.86
Minimum concentration	$c_{\min}$		0.14

Supplementary Reference

1. Jia, H., et al. Nanostructured $ZnFe_2O_4$ as Anode Material for Lithium-Ion Batteries: Ionic Liquid-Assisted Synthesis and Performance Evaluation with Special Emphasis on Comparative Metal Dissolution. *Acta Chim. Slov.* **63,** 470-483 (2016).